

Thermoelectric, magnetotransport, and ultrafast dynamics of bismuth telluride thin films grown using pulsed laser deposition: Effects of substrate temperature and post-annealing

Le Thi Cam Tuyen^{a,b}, Bih-Show Lou^a, Jyh-Wei Lee^c, Ngo Ngoc Uyen^d, Phuoc Huu Le^{e,f,*}, Chien-Neng Liao^g, Chih-Wei Luo^{h,i,j,k}, Jiunn-Yuan Linⁱ

^a Chemistry Division, Center for General Education, Chang Gung University, Taoyuan, Taiwan.

^b Department of Chemical Engineering and Biotechnology, Tatung University, Taipei City 104327, Taiwan

^c Department of Materials Engineering, Ming Chi University of Technology, New Taipei City, Taiwan

^d Department of Physics and Biophysics, Faculty of Basic Sciences, Can Tho University of Medicine and Pharmacy, Vietnam

^e Center for Plasma and Thin Film Technologies, Ming Chi University of Technology, New Taipei City 243303, Taiwan.

^f International PhD Program in Plasma and Thin Film Technology, Ming Chi University of Technology, New Taipei City 243303, Taiwan

^g Department of Materials Science and Engineering, National Tsing-Hua University, Hsinchu 30013, Taiwan

^h Department of Electrophysics, National Yang Ming Chiao Tung University, Hsinchu 30010, Taiwan

ⁱ Institute of Physics, National Yang Ming Chiao Tung University, Hsinchu 30010, Taiwan

^j Faculty of Electrical and Electronics Engineering, Ton Duc Thang University, Ho Chi Minh City 758307, Vietnam

^k National Synchrotron Radiation Research Center, Hsinchu 30076, Taiwan

Email: phle@mail.mcut.edu.tw

Abstract

n-Type Bi₂Te₃ and Bi₄Te₅ thin films were grown on SiO₂/Si substrates via pulsed laser deposition (PLD) at substrate temperatures (T_s) ranging from 25°C to 350°C under 220 mTorr He. Film morphology evolved from nanoparticles to layered hexagonal platelets with increasing T_s , accompanied by a shift in preferred orientation from (015) to highly (001)-oriented textures. Composition varied from Te-rich at low T_s to Te-deficient at 350°C. Near-stoichiometric and (001)-textured Bi₂Te₃ thin films deposited at 250–300°C exhibited reduced carrier concentration ($\sim 9.5 \times 10^{19} \text{ cm}^{-3}$), significantly enhanced mobility

(up to $81.2 \text{ cm}^2/\text{V}\cdot\text{s}$), and a maximum thermoelectric (TE) power factor (PF) of $20.0 \mu\text{W}\cdot\text{cm}^{-1}\cdot\text{K}^{-2}$. To further enhance TE performance, Bi_2Te_3 films grown at 200, 250, and 300°C were in-situ annealed in helium gas at 220 mTorr for 60 minutes at annealing temperatures (T_A) of 200, 250, 300, and 350°C . Simultaneous tuning of T_S and T_A revealed a processing window for optimized PFs, achieving a peak value of $23.8 \mu\text{W}\cdot\text{cm}^{-1}\cdot\text{K}^{-2}$ for the film grown at 250°C and annealed at 250°C — a 19% improvement over the as-deposited counterpart. Additionally, low-temperature transport measurements exhibited two-dimensional weak antilocalization behavior in the optimized TE Bi_2Te_3 thin film, suggesting the presence of topological surface states. Ultrafast spectroscopy further revealed coherent optical and acoustic phonon modes at 1.87 THz and 37.3 GHz, respectively.

Keywords: Bi_2Te_3 , pulsed laser deposition, thermoelectrics, magnetotransport, pump-probe.

1. Introduction

Solid-state thermoelectric (TE) devices provide a direct means to convert waste heat into electricity or function as solid-state coolers, offering advantages such as no moving parts, silent operation, high reliability, and autonomous functionality [1, 2, 3]. Growing interest in miniaturized TE systems has driven research toward thin-film devices, which offer superior integration with microelectronics and semiconductor processing [4, 5, 6]. Compared to bulk devices, thin-film TEs (thickness $\leq 10 \mu\text{m}$) demonstrate faster thermal response ($\sim 15\text{--}20 \mu\text{s}$ vs. 0.35 s for bulk), and can sustain significantly higher heat pumping densities ($700\text{--}720 \text{ W}/\text{cm}^2$ vs. $10\text{--}40 \text{ W}/\text{cm}^2$) [1, 6, 7].

The performance of TE materials is evaluated by the dimensionless figure of merit, $ZT = \sigma S^2 T / \kappa$, where σ is electrical conductivity, S is the Seebeck coefficient, T is absolute temperature, and κ is thermal conductivity. Achieving a high ZT requires maximizing the power factor ($\text{PF} = \sigma S^2$) and minimizing κ . However, optimizing ZT is challenging due to the coupling between TE parameters [2]. The inverse dependence of S on carrier concentration (n), as $|S| \sim n^{-2/3}$ approximately [2], poses a fundamental challenge to enhancing the PF. Simultaneously, the Wiedemann–Franz law, which links electrical

conductivity (σ) to electronic thermal conductivity, constrains improvements in the σ/κ ratio by coupling charge and heat transport. Extensive research efforts to enhance ZT have predominantly focused on two key strategies [8]: (i) reducing the lattice thermal conductivity by incorporating rattler atoms into cage-like structures [9], embedding nanoparticles into the matrix [10], or applying nanostructuring techniques to conventional materials [11, 12]; and (ii) improving the power factor (PF) through optimized carrier and band structure engineering [8, 13]. This study focuses on the latter strategy, aiming to significantly boost the PF.

Among TE materials, Bi_2Te_3 and its alloys remain the most widely used near room temperature owing to their balanced σ , S , and κ values, typically yielding a ZT value close to 1 [8, 14, 15, 16, 17]. Bi_2Te_3 -based modules have found applications in automotive waste heat recovery [18], medical cooling devices [19, 20], and wearable energy harvesters [21]. For instance, micro-TE coolers based on Bi_2Te_3 thin films have been implemented for thermal management in integrated circuits [6], while TEGs have been developed for harvesting body heat [21].

Bi_2Te_3 -based thin films and their TE properties have been extensively investigated using various fabrication techniques, including sputtering [22, 23, 24], thermal evaporation [4], low pressure chemical vapour deposition [25], spin-coating with co-reduction [26], and pulsed laser deposition (PLD) [27, 28, 29, 30]. Among these techniques, pulsed laser deposition (PLD) offers distinct advantages for Bi_2Te_3 thin film synthesis: (i) stoichiometric transfer from target to substrate via high instantaneous ablation rates, enabling precise compositional control [31]; (ii) high kinetic energy of ablated species (10–100 eV) promoting dense, highly crystalline films with reduced porosity [32]; (iii) independent control of substrate temperature and deposition pressure for systematic growth-parameter optimization [33]; and (iv) compatibility with diverse processing atmospheres and substrate materials. Despite its limitation to smaller substrate sizes (cm-scale), PLD's capability to produce high-quality, highly textured films makes it well-suited for fundamental thermoelectric property studies [30, 34].

A key advantage of TE thin films lies in their fine granular microstructure, which enhances phonon scattering at grain boundaries, thereby reducing lattice thermal conductivity and improving ZT [35]. Among growth parameters, the substrate temperature (T_S) plays a critical role in controlling microstructure, crystallinity, and defect density, directly influencing the PF [36]. Post-deposition annealing further enhances TE performance by increasing grain size, reducing defect levels, and improving carrier mobility, which collectively boost σ and PF while minimizing κ [37, 38]. Morgan *et al.* [14] reported a PF of $2.2 \mu\text{W}\cdot\text{cm}^{-1}\text{K}^{-2}$ in Bi-Te thin films annealed at 300°C on flexible substrates, demonstrating the efficacy of thermal treatment for performance enhancement. However, systematic dual-parameter mapping of the (T_S , T_A) processing space to identify optimal thermoelectric performance windows remains underexplored in PLD-grown Bi_2Te_3 thin films.

Beyond thermoelectrics, Bi_2Te_3 is also a well-known 3D topological insulator (TI), possessing conducting surface states protected by time-reversal symmetry [39, 40]. The topological surface states (TSSs) in TIs are of interest for spintronic and quantum computing applications [39, 40]. Notably, the electronic structure underlying TSSs (characterized by Dirac-cone dispersion and high surface carrier mobility) is intimately connected to the thermoelectric transport properties, as both depend on the material's band structure, defect density, and carrier scattering mechanisms [41].

TSSs can be probed via 2D weak anti-localization (WAL) behavior in magnetotransport studies [42, 43, 44]. However, Bi_2Se_3 and Bi_2Te_3 are typically heavily doped as a result of vacancies and anti-site defects, leading to dominant bulk conduction that significantly obscures the detection of TSSs [45, 46]. Therefore, identifying processing conditions that simultaneously optimize thermoelectric performance (requiring controlled carrier concentration and high mobility) and preserve accessible TSSs (requiring suppression of bulk conduction) represents a critical challenge. Complementary characterization via magnetotransport measurements (probing TSS contribution [42, 43, 44]) and ultrafast pump-probe spectroscopy (revealing carrier-phonon coupling and surface-vs-bulk relaxation dynamics [47] – as demonstrated in Bi_2Se_3 [46, 48], Bi_2Te_3 [49, 50], and $\text{Bi}_2\text{Se}_2\text{Te}$ [51, 52]) enables

comprehensive evaluation of both quantum transport and dynamical properties in optimized thermoelectric films.

Despite extensive studies on temperature-dependent optimization of Bi_2Te_3 thin films, prior PLD investigations have mainly treated substrate temperature (T_S) and post-annealing temperature (T_A) separately, without systematically mapping the combined (T_S , T_A) processing space. As a result, simultaneous optimization of thermoelectric performance, topological surface state accessibility, and carrier-phonon dynamics in PLD-grown Bi_2Te_3 thin films remains largely unexplored. In this work, n-type Bi_2Te_3 thin films were grown by PLD at T_S from room temperature to 350°C , followed by in-situ post-annealing in helium (220 mTorr) at $T_A = 200\text{--}350^\circ\text{C}$ for 60 minutes. This dual tuning of T_S and T_A reveals a processing window that maximizes the power factor. The optimized film is then examined by low-temperature magnetotransport to probe TSSs and by ultrafast pump–probe spectroscopy to resolve carrier–phonon dynamics. By correlating processing conditions with thermoelectric, structural, quantum transport, and ultrafast dynamical properties, this study provides guidelines for designing high-performance Bi_2Te_3 -based thin-film thermoelectrics.

2. Experimental Details

n-Type Bi_2Te_3 thin films were fabricated on SiO_2 (500 nm)/Si (100) substrates (size of $2 \times 2 \text{ cm}^2$) using pulsed laser deposition (PLD) across a substrate temperature (T_S) range of $25\text{--}350^\circ\text{C}$. The chamber was evacuated to a base pressure below 3×10^{-6} Torr using a mechanical pump followed by a turbomolecular pump. The deposition was conducted in a 220 mTorr helium ambient. Helium was selected as the ambient gas due to its superior thermal conductivity (0.152 vs. 0.018 W/m·K for Ar) enabling uniform substrate heating [53], chemical inertness preventing oxidation, and low atomic mass minimizing re-sputtering damage. The substrate temperature was limited to 350°C to maintain the Bi_2Te_3 phase; higher temperatures induce Bi_4Te_5 formation via preferential Te re-evaporation (see Figs. 1-2). A KrF excimer laser ($\lambda = 248 \text{ nm}$) operating at 10 Hz delivered 15–20 ns pulses at a fluence of 3.8 J/cm^2

per pulse, targeting a stoichiometric polycrystalline Bi_2Te_3 source. The target-to-substrate distance was fixed at 40 mm. Each deposition consisted of 15,000 laser pulses over 25 minutes, resulting in a film growth rate of approximately 0.46 Å per pulse.

Prior to deposition, the chamber was evacuated to a base pressure of 2×10^{-6} Torr, followed by helium backfilling and stabilization via differential pumping. To enhance thermoelectric performance, films deposited at 200, 250, and 300°C were subjected to in-situ post-deposition annealing for 60 minutes within the PLD chamber under 220 mTorr helium at annealing temperatures (T_A) of 200, 250, 300, and 350°C.

The structural properties and crystallographic orientation were analyzed by X-ray diffraction (XRD, Bruker D8) using Cu $K\alpha$ radiation ($\lambda = 1.5406$ Å) in a 2θ – ω scan mode. Film morphology and thickness were examined by field-emission scanning electron microscopy (FE-SEM, JEOL JSM-6500) in both top-view and cross-sectional configurations. Elemental compositions were determined via energy-dispersive X-ray spectroscopy (EDS, Oxford Instruments) integrated with the SEM system. Measurements were performed at 15 kV accelerating voltage, with a 90-second acquisition time and dead time between 22% and 30%. Atomic percentages were calculated by averaging data from five randomly selected surface regions.

X-ray photoelectron spectroscopy (XPS, ThermoVG 350) was employed to evaluate surface composition and chemical states after five days of atmospheric exposure. Measurements were carried out using a Mg $K\alpha$ source (1253.6 eV, 300 W), with calibration to the C1s peak at 284.6 eV. Spectral fitting was conducted using XPSPEAK 4.1 software, employing Gaussian–Lorentzian line shapes and Shirley background subtraction. The in-plane electrical conductivity, carrier concentration, and Hall mobility were measured at room temperature using a van der Pauw configuration (Bio-Rad HL5500PC), with indium contacts ensuring reliable ohmic behavior.

The in-plane Seebeck coefficient was measured at room temperature using a longitudinal DC steady-state method ($S = -\Delta V/\Delta T$) [54]. A programmable power supply controlled via LabVIEW

established a stable temperature gradient ($\Delta T = 0.9 - 1.8$ K) across the film, monitored by T-type thermocouples (± 0.1 K accuracy). The resulting thermoelectric voltage (ΔV) was recorded using a digital voltmeter with high input impedance (> 10 M Ω) to ensure negligible current flow. The Seebeck coefficient was extracted from the linear slope of multiple ΔV vs. ΔT measurements, averaged to ensure reproducibility. Measurement uncertainty was estimated at ± 3 μ V/K.

Temperature-dependent magnetotransport properties were assessed using a standard four-probe configuration in a physical property measurement system (Quantum Design) from 2 to 10 K. Silver paste was used for electrical contacts. Measurements were conducted with the magnetic field aligned along out-of-plane direction, while both current and thermal gradient were applied parallel to the film plane. Ultrafast carrier and phonon behaviors at room temperature were investigated using a dual-wavelength femtosecond pump–probe technique. A Ti:sapphire laser system, operating at 5.2 MHz with 70 fs pulse duration, provided excitation pulses at 400 nm (3.1 eV) and probing pulses at 800 nm (1.55 eV). During the measurements, the pump and probe fluences were set to 200 μ J/cm² and 9.8 μ J/cm², respectively.

3. Results and Discussion

3.1. Substrate temperature- dependent structural, compositional, electrical, and thermoelectric properties of Bi-Te thin films

Figure 1(a) presents the X-ray diffraction (XRD) patterns of Bi-Te thin films prepared at various T_S . For $T_S \leq 300$ °C, the films exhibited the Bi₂Te₃ phase and highly c-axis preferred orientation, characterized by diffraction peaks at 8.8°, 17.5°, 27.7°, 44.7°, 54.4°, and 64.4°, corresponding to the (003), (006), (015), (0015), (0018), and (0021) planes, respectively, consistent with JCPDS card No. 00-015-0863. When T_S was increased to 350 °C, the films transition to the Bi₄Te₅ phase, displaying sharp and well-defined peaks at 18.5°, 27.5°, 38.4°, 45.5°, and 57.1°, corresponding to the (0011), (109), (1018), (0027) and (0032) planes, respectively. This phase transition at 350°C was attributed to the Te-deficient composition (by 9 at. %, Fig. 2), due to the sufficient re-evaporation of volatile Te element at the elevated temperature. Additionally, this high temperature increased the ad-atoms mobility, leading to the

structural reorganization to form to Bi_4Te_5 phase. Researches have shown that higher growth temperatures can induce a transition from the Bi_2Te_3 phase to other bismuth-rich phases such as Bi_4Te_5 , BiTe , $\text{Bi}_{10}\text{Te}_9$, Bi_4Te_3 , and Bi_3Te_3 , as the thermodynamic stability of these phases varies with temperature [55].

As shown in Fig. 1b, the crystallite size distribution was extracted from the XRD data using the Scherrer equation: $D = \frac{K\lambda}{\beta \cos\theta}$, where D is the average crystallite size, $K = 0.9$ is the shape factor, $\lambda = 1.5406 \text{ \AA}$ is the X-ray wavelength, β is the full width at half maximum (FWHM) of the diffraction peak, and θ is the Bragg angle. The data reveal a clear temperature-dependent trend: crystallite size increases with T_S , peaking at 250°C , and then declines at higher temperatures. At lower T_S ($25\text{--}120^\circ\text{C}$), limited atomic mobility results in smaller crystallites ($16.5\text{--}30.0 \text{ nm}$). As T_S rises above 120°C , enhanced atomic diffusion facilitates crystallite coalescence, reaching a maximum size of 81.0 nm at 250°C . This behavior is consistent with prior reports, such as Kim *et al.* [56], who observed similar crystallite growth trends in bismuth telluride thin films with increasing T_S . These results align with classical nucleation and growth theories, where thermal activation drives coalescence and grain enlargement [27, 30, 34]. Beyond 250°C , crystallite size decreases, likely due to increased adatom re-evaporation, or defect generation from thermal stress, which collectively hinder further grain growth [57, 58]. Thus, the observed peak at 250°C represents an optimal T_S for promoting crystallite growth, which is critical for tuning the microstructural and functional properties of the thin films.

Figure 2 illustrates the dependence of Te concentration (at.%) on T_S , revealing a distinct decline in Te content with increasing T_S . At lower T_S , the films exhibit a slightly Te-rich composition, with an excess of $4.7 \text{ at.}\%$ at 25°C and $3.2 \text{ at.}\%$ at 120°C relative to the stoichiometric ratio (indicated by the dashed blue line in Fig. 2). As T_S increases to 200°C , the composition approaches near-stoichiometry ($\approx 60.8 \text{ at.}\%$). Beyond this point, a gradual shift toward Te deficiency (by $\sim 1.1\text{--}1.2 \text{ at.}\%$) is observed at

250–300°C, followed by a sharp decrease to 50.7 at.% at 350°C, where the Bi₄Te₅ phase emerges (Fig. 1a).

This evolution in composition with T_S is governed by the intrinsic differences in vapor pressures and sticking coefficients of Bi and Te. At low T_S (< 200 °C), both elements exhibit relatively high sticking probabilities [59] and the limited surface diffusion and re-evaporation of ablated species during PLD growth promote retention of the more volatile Te, resulting in a slightly Te-rich film. As the T_S rises (≥ 250 °C), however, the sticking coefficient of Te decreases markedly [59], while its high vapor pressure ($P_{Te}/P_{Bi} \approx 10^5$ at 300 °C) [27] promotes preferential Te re-evaporation from the heated substrate surface. The combination of reduced Te sticking and accelerated re-evaporation leads to a monotonic suppression of Te incorporation at elevated T_S , resulting in a progressive transition from Te-rich to Te-deficient composition as observed experimentally.

Figure 3 shows the morphological evolution of Bi-Te thin films grown at different T_S from 25°C to 350°C. The top-view and cross-sectional SEM images provide insights into grain size, surface morphology, and film thickness. At 25°C and 120°C (Figs. 3a,b), the films exhibit small, densely packed grains of nanoflower-like columnar structures formed with minimal grain coarsening and shadowing growth [60]. As T_S increases to 200°C (Fig. 3c), the grains become significantly larger, suggesting enhanced atomic mobility and grain coalescence. The grains have rock-like shapes, the film has thickness of 600 nm and compact structure (Fig. 3c). Thin films deposited at 250 and 300°C exhibited distinct layered architectures composed of hexagonal platelets with strong c-axis texturing. This structural preference is likely driven by the anisotropic bonding nature of Bi₂Te₃, which promotes much faster crystal growth parallel to the basal planes compared to the c-axis direction [61]. Meanwhile, the layered structure was grown owing to layered structural nature of Bi₂Te₃ and high diffusion mobility of adatoms at the elevated T_S -growth. At 350°C, the film exhibited a rougher surface with larger, polyhedron- and rock-like particles. This morphological change can be attributed to the formation of the Bi₄Te₅ phase, whose different crystal structure from Bi₂Te₃ disrupts the typical anisotropic growth mode. Moreover,

the elevated T_s enhances adatom surface mobility and promotes re-evaporation, leading to island growth, grain coalescence, and surface roughening via step bunching or Ostwald ripening—where larger grains grow at the expense of smaller ones—ultimately resulting in a coarser and less uniform film morphology. [Figure 4](#) illustrates the growth mechanisms corresponding to the morphological evolution seen in the SEM images. At low substrate temperatures (25–120 °C, $T_s/T_m = 0.04 - 0.21$), limited adatom mobility and shadowing effects result in a quenched growth regime, forming columnar or rice-like grains with (015) orientation. As T_s increases to 200 °C, moderate surface diffusion facilitates polycrystalline growth with improved grain connectivity. In the intermediate T_s range of 250–300 °C ($T_s/T_m = 0.43-0.51$), sufficient adatom mobility and the intrinsically layered structure of Bi_2Te_3 , combined with its anisotropic bonding, promote the formation of well-aligned hexagonal platelets with strong (001) orientation. At 350 °C ($T_s/T_m = 0.60$), the onset of surface and bulk diffusion, coupled with increased Te re-evaporation, disrupts the anisotropic growth mode. This leads to island growth, grain coalescence, and surface roughening, ultimately resulting in the formation of Bi_4Te_5 with rock-like and polyhedral morphologies.

XPS analysis of Bi 4f and Te 3d core levels was conducted to assess the surface composition and oxidation states of the 250 °C- Bi_2Te_3 thin film after five days of air exposure. As shown in [Fig. 5a](#), the Bi 4f spectrum was deconvoluted into two main characteristic peaks of Bi_2Te_3 , corresponding to Bi 4f_{7/2} at 157.2 eV and Bi 4f_{5/2} at 162.5 eV. In addition, two smaller peaks observed at 158.5 eV and 163.8 eV are attributed to oxidized bismuth species (Bi_2O_3). Similarly, in [Fig. 5b](#), the Te 3d region exhibits a clear doublet with peaks at 572.0 eV (Te 3d_{5/2}) and 582.3 eV (Te 3d_{3/2}), confirming the presence of Te in Bi_2Te_3 , along with additional TeO_2 peaks at 574.5 eV and 584.8 eV. The results confirm Bi_2Te_3 formation with evident surface oxidation after air exposure. The observed spectral features are in good agreement with previously reported XPS data for Bi_2Te_3 single crystals [\[62\]](#), hydrothermally synthesized nanostructures [\[63\]](#), and electrodeposited thin films [\[64\]](#).

To evaluate the effect of *in-situ* thermal annealing during PLD, a Bi₂Te₃ film deposited at 250°C and subsequently annealed at $T_A = 300^\circ\text{C}$ for 1 h in 220 mTorr helium was examined by XPS. As shown in Figs. 5c,d, the spectrum exhibits dominant Bi 4f and Te 3d peaks of Bi₂Te₃, along with evident oxide components – Bi₂O₃ (158.6, 163.9 eV) and TeO₂ (574.9, 585.9 eV) – similar to the non-annealed film (Figs. 5a,b). Quantitative analysis of the oxide-to-Bi₂Te₃ peak area ratios confirms that the Bi₂O₃ and TeO₂ contents are comparable for both films. This indicates that in-situ annealing in a deposition chamber evacuated to high vacuum ($< 3 \times 10^{-6}$ Torr) and subsequently maintained at 220 mTorr helium does not significantly increase the surface oxidation of Bi₂Te₃.

Figure 6 presents the influence of T_S on the electrical and thermoelectric properties of Bi–Te thin films. As shown in Fig. 6a, the electron concentration (n) decreased progressively from 3.1×10^{20} to $0.48 \times 10^{20} \text{ cm}^{-3}$ with increasing T_S from 25°C to 300°C, corresponding to the Bi₂Te₃ phase. This reduction is attributed to the suppression of Te-related donor defects, such as antisite Te_{Bi} [65], which has a low formation energy (~ 0.5 eV) under Te-rich conditions [66, 67], and a decrease in Te vacancies as the film composition approaches stoichiometry (see Fig. 2) [68]. At 350°C, the carrier concentration (n) increased sharply to $7.1 \times 10^{20} \text{ cm}^{-3}$, which is associated with the formation of a Bi₄Te₅ phase with a stoichiometry of 44.4 at.% Bi and 55.6 at.% Te. This composition reflects a notable Te-deficiency of 4.8 at.%, which likely promotes the formation of donor defect of Te vacancies [65, 68], thereby enhancing n -type conductivity [66, 67].

The electron mobility (μ) increased markedly from 0.4 cm²/V·s at 25°C to a maximum of 81.2 cm²/V·s at 250°C, followed by a decline to 69.3 cm²/V·s at 300°C and 25.9 cm²/V·s at 350°C. This trend is governed by the combined effects of grain size (D) and n , where μ is positively correlated with D and inversely related to n [65, 69]. At low T_S , limited grain growth and high defect densities lead to pronounced grain boundary and ionized impurity scattering, resulting in poor carrier mobility [70]. In contrast, films deposited at 250–300°C exhibit larger grains and low n associated with near-

stoichiometric Bi₂Te₃ composition (Figs. 1b and 2), yielding improved μ [70]. The significant drop in μ at 350°C is ascribed to enhanced impurity scattering due to the high n and the presence of surface roughness and voids (Fig. 3). Consequently, the electrical resistivity ($\rho = 1/n\mu e$, with $e = 1.6 \times 10^{-19}$ C) remained low, ranging from 0.33 to 1.86 m Ω ·cm for films grown at T_S between 200 and 350°C (Fig. 6a), reflecting a favorable balance between carrier concentration and mobility in this temperature window.

The relationship between the Seebeck coefficient (S) and carrier concentration (n) in metals and degenerate semiconductors (under the parabolic band and energy-independent scattering approximation) is described by [2]:

$$S = \frac{8\pi^2 k_B^2}{3eh^2} m^* T \left(\frac{\pi}{3n}\right)^{2/3} \quad (1)$$

where m^* is the carrier effective mass, T is temperature, and n is the electron concentration. As shown in Fig. 6b, the absolute Seebeck coefficient ($|S|$) exhibits a clear inverse dependence on n , decreasing from ~ 133.4 μ V/K at 0.48×10^{20} cm⁻³ to 37.3 μ V/K at 7.1×10^{20} cm⁻³, consistent with the theoretical $|S| \propto m^* n^{-2/3}$ behavior typical of degenerate semiconductors.

In this work, fitting the experimental data using Eq. (1) (the Pisarenko relation) yielded an effective mass of $m^* \approx 1.0m_0$. In thermoelectric materials, the transport-derived m^* is not a fixed band parameter – it depends on valley degeneracy, band anisotropy, and can be significantly elevated by thin-film dimensionality and defect-induced band distortion, while its apparent value also shifts with carrier concentration and the assumed scattering model [71, 72, 73]. Correspondingly, a wide range of reported m^* values exists for Bi₂Te₃ and related materials: $m^* = 0.19m_0$ for Bi₂Te₃ bulk [74], $m^* = 0.5m_0 - 0.6m_0$ for Bi_{0.5}Sb_{1.5}Te₃ thin films at 100 K [75], and $m^* = 0.902m_0$ for Bi₂Se₃ nanosheets synthesized via the polyol method [71]. The effective masses of holes ($1.26m_0$) and electrons ($1.07m_0$) in Bi₂Te₃ bulk have also been reported [76], while $m^* \approx 1.06m_0$ for both n -type and p -type Bi₂Te₃ has been reviewed [77]. More recently, $m^* = 1.0 - 2.0m_0$ has been extracted for homo-layer flexible Bi₂Te_{2.85}Se_{0.15} films grown

via combined magnetron sputtering and vacuum thermal evaporation [78], which is fully consistent with our fitted value of $m^* = 1.0m_0$.

Under Bi-rich growth conditions, Bi_2 bilayers may intercalate between the quintuple-layered $\text{Te}^{(1)}\text{--Bi--Te}^{(2)}\text{--Bi--Te}^{(1)}$ structure, forming $\text{Bi}_2\text{--Bi}_2\text{Te}_3$ superlattice-like films with carrier concentrations approaching $n \sim 10^{21} \text{ cm}^{-3}$ [79]. These structural modifications can strongly reshape the band structure, converting the conduction band from single-valley to multivalley, and have been reported to yield markedly higher m^* values of 2.78–3.90 m_0 [79]. Importantly, the moderately enhanced $m^* = 1.0m_0$ obtained in this work is likely beneficial, as it increases the density-of-states effective mass without severely degrading mobility, thereby supporting the experimentally observed high Seebeck coefficient even at elevated carrier concentrations ($\sim 10^{20} \text{ cm}^{-3}$).

A. Novitskii and T. Mori [73] systematically reexamined the Pisarenko relation and demonstrated that, although traditionally associated with the non-degenerate limit, it remains reasonably accurate into the partially degenerate regime, with its applicability range depending on the dominant scattering mechanism. Comparison with full numerical solutions of the Fermi integrals indicates that the commonly used degenerate approximation may underestimate the density-of-states effective mass at high $|S|$ values ($|S| \gtrsim 150 \mu\text{V K}^{-1}$), whereas the Pisarenko formulation often provides improved accuracy in this range. Further analysis also emphasizes that the transport-derived effective mass should be interpreted as an apparent parameter reflecting valley degeneracy, band anisotropy, and scattering effects rather than a purely intrinsic band mass. Accordingly, the extracted m^* in this work is treated as an effective transport descriptor for comparison with related Bi_2Te_3 systems.

Figure 6c illustrates the T_S -dependent evolution of σ , S , and PF ($= S^2\sigma$). As T_S increases from 25°C to 250°C, σ rises sharply from 20.2 to 1244.7 S/cm, then declines to 538.0 S/cm at 300°C, before peaking at 2960.1 S/cm at 350°C due to phase transition and the highest n . Meanwhile, $|S|$ shows a non-monotonic

trend: it increases from 73.6 $\mu\text{V/K}$ at 25°C to a maximum of 133.4 $\mu\text{V/K}$ at 300°C, then drops to 37.3 $\mu\text{V/K}$ at 350°C (Fig. 6c), reflecting the change in n and scattering mechanisms.

The highest room temperature PF of 20.0 $\mu\text{W/cm}\cdot\text{K}^2$ was achieved at $T_S = 250^\circ\text{C}$, where an optimal combination of high conductivity and moderately large Seebeck coefficient ($S = -126.8 \mu\text{V/K}$) is obtained (Fig. 6c). Beyond 300°C, the sharp drop in $|S|$ outweighs gains in σ , leading to a net decrease in PF. These findings highlight 250°C as the optimal deposition temperature for high TE performance in Bi_2Te_3 thin films under a helium gas pressure of 220 mTorr.

The electronic thermal conductivity (κ_e) of the Bi–Te films was estimated using the Wiedemann–Franz law ($\kappa_e = \sigma LT$, with $L = 2.4 \times 10^{-8} \text{ W } \Omega \text{ K}^{-2}$ for degenerate carriers under elastic scattering). As shown in Fig. 6d, κ_e increases markedly with T_S , from 0.015 $\text{W}\cdot\text{m}^{-1}\text{K}^{-1}$ at 25°C to 2.13 $\text{W}\cdot\text{m}^{-1}\text{K}^{-1}$ at 350°C, mirroring the trend in σ (Fig. 6a). At low T_S (25–120°C), the nanocolumnar “nanoflower-like” microstructure and small grain size ($\leq 30 \text{ nm}$) induce severe carrier scatterings ($\mu \leq 2.23 \text{ cm}^2/\text{Vs}$), yielding low σ ($\leq 94.4 \text{ S cm}^{-1}$) and thus minimal κ_e . Increasing T_S to 200–300 °C produces well-textured, layered hexagonal platelets with larger grains (68.8–80.9 nm), enhancing carrier mobility (69.3–81.3 cm^2/Vs) and, consequently, rising κ_e to 0.387 – 0.896 $\text{Wm}^{-1}\text{K}^{-1}$. At 350°C, the emergence of Bi_4Te_5 leads to a very high carrier concentration ($n \approx 7.15 \times 10^{20} \text{ cm}^{-3}$) and reduced μ (25.9 cm^2/Vs), resulting in a high $\sigma = 2960.1 \text{ S cm}^{-1}$ and the peak κ_e of 2.13 $\text{W}\cdot\text{m}^{-1}\text{K}^{-1}$.

The intermediate κ_e values (0.387, 0.483, and 0.896 $\text{Wm}^{-1}\text{K}^{-1}$) obtained for the Bi_2Te_3 deposited at T_S of 200 – 300°C are comparable to reported $\kappa_e \approx 0.4 \text{ W m}^{-1} \text{ K}^{-1}$ for nanocrystalline $\text{Bi}_2\text{Te}_{2.7}\text{Se}_{0.3}$ films [80].

3.2. Thermoelectric properties of Bi-Te thin films grown at various substrate temperatures and annealing temperatures

Figure 7 presents the XRD patterns of the Bi_2Te_3 film grown at $T_S = 250^\circ\text{C}$ and subsequently subjected to *in-situ* thermal annealing ($T_A = 200\text{--}350^\circ\text{C}$). Consistent with the T_S -dependent results (Fig.

1), all annealed films retain a strong *c*-axis preferred orientation, exhibiting dominant (001) reflections along with minor non-(001) peaks such as (015), (205), and (0 2 10). For $T_A = 200\text{--}300^\circ\text{C}$, only the single-phase Bi_2Te_3 was observed. In contrast, annealing at 350°C led to the emergence of a secondary Bi_4Te_5 phase, confirmed by the appearance of the Bi_4Te_5 (0 0 11) peak at 18.1° and (0 0 27) peak at 45.0° (see insets of Fig. 7a).

To further assess the effect of thermal annealing on the crystal structure, the average *c*-axis lattice constant was extracted from the (0 0 6) and (0 0 15) reflections using the hexagonal unit cell relation (Eq. 2):

$$\frac{1}{d_{hkl}^2} = \frac{4}{3} \left(\frac{h^2 + hk + k^2}{a^2} \right) + \frac{\ell^2}{c^2} \quad (2)$$

The *c*-axis lattice constants were 30.34 \AA for the as-grown and $200\text{--}250^\circ\text{C}$ annealed Bi_2Te_3 films, slightly decreasing to 30.32 \AA at $T_A = 300^\circ\text{C}$ and 30.26 \AA at $T_A = 350^\circ\text{C}$. All of these values are lower than the standard lattice constant of 30.44 \AA for Bi_2Te_3 powder (JCPDS 82-0358), which is commonly attributed to the formation of Te_{Bi} antisite donor defects under Te-rich conditions [81]—due to the smaller atomic radius of Te (1.4 \AA) compared to Bi (1.6 \AA)—as well as the presence of Te vacancies (V_{Te}) under Te-deficient conditions.

The grain size and microstrain of the Bi_2Te_3 films were evaluated using the Williamson–Hall method [82], as expressed in Eq. (3):

$$\beta \cos \theta = \frac{K\lambda}{D_\beta} + 4\varepsilon \sin \theta \quad (3)$$

where β is the full width at half maximum (FWHM) of the selected diffraction peak at 2θ , K is the Scherrer factor (~ 0.9), λ is the wavelength of the Cu K_α radiation (0.15406 nm), D_β is the nanograin size, and ε is the microstrain. The grain size (D_β) and microstrain (ε) are respectively extracted from the intercept and slope of the linear fit in the $\beta \cos \theta$ versus $4 \sin \theta$ plot. The evolution of these parameters with annealing temperature (T_A) is presented in Fig. 7(c). The microstrain values ($0.141\text{--}0.197\%$) indicate that

the observed lattice distortion mainly originates from point-defect incorporation rather than macroscopic stress effects. As shown in Fig. 7c, microstrain decreases with increasing T_A from 200 to 300°C, indicating defect relaxation via diffusion at the annealing temperatures. However, it rises considerably to 0.197% at $T_A = 350^\circ\text{C}$, which correlates with the onset of Bi_4Te_5 secondary phase formation. Meanwhile, in Fig. 7c, grain size was 76.1 nm for the as-grown film exhibits; it remains unchanged at $T_A = 200^\circ\text{C}$ ($T_A < T_S$), then increases to 80.7 nm at 250°C and peaks at 92.0 nm at 300°C. At $T_A = 350^\circ\text{C}$, the grain size drops to 74.4 nm, arising from the emergence of secondary Bi_4Te_5 phase.

To further enhance the TE property, the Bi_2Te_3 thin films grown at T_S of 200, 250, and 300°C were subjected to *in-situ* thermal annealing (T_A) at 200, 250, 300°C, and 350°C for 60 minutes in 220 mTorr helium atmosphere inside the PLD chamber. The T_A - dependent morphology change is presented in Figure 8. For the films deposited at $T_S = 200^\circ\text{C}$, a pronounced columnar rock-like morphology is observed. In comparison, the films grown at $T_S = 250^\circ\text{C}$ and subsequently annealed at $T_A = 250$ and 300°C exhibit a mixed surface morphology, characterized by rock-like grains together with poorly defined hexagonal features, accompanied by relatively dense and compact layered structures. Meanwhile, the films deposited at $T_S = 300^\circ\text{C}$ show a well-developed layered morphology consisting of hexagonal platelets, indicating enhanced crystalline ordering and anisotropic growth at the higher substrate temperature. These morphologies remain unchanged with annealing at $T_A = 200\text{--}300^\circ\text{C}$, though a slight increase in grain size is noted with increasing T_A . The increase in grain size with higher T_A is attributed to enhanced atomic mobility, which promotes grain growth and recrystallization [57], reducing grain boundary density, and thus can manipulate carrier transport in the Bi_2Te_3 films.

After thermal annealing at 350°C, both Bi_2Te_3 films initially grown at $T_S = 200^\circ\text{C}$ and 300°C exhibit a marked morphological transformation. The distinct rock-like columnar grains ($T_S = 200^\circ\text{C}$) and layered hexagonal platelets ($T_S = 300^\circ\text{C}$) evolve into a denser, more compact microstructure with indistinct grain boundaries, indicating significant grain merging. This morphological change suggests

the onset of partial recrystallization, driven by enhanced atomic diffusion at higher temperatures near 60% of Bi₂Te₃'s melting point ($T_m \approx 585^\circ\text{C}$). Such thermal energy enables grain boundary migration and coalescence, reducing inter-granular voids and forming a more continuous film. Densification behavior has been observed in Bi₂Te₃ films subjected to thermal and laser treatments [83], as well as in hot-pressed Bi₂Se_{0.21}Te_{2.79} bulk materials following thermal annealing and electrical stressing [84].

Figure 9 shows the evolution of PF as a function of T_S and T_A , compared to as-deposited films. Thermal annealing notably enhanced PF values in several cases, including films deposited at 200°C and annealed at 200 and 250°C; and those grown at 300°C with the same annealing conditions. Notably, the 250°C-grown-250°C-annealed film exhibited a peak PF of $23.8 \mu\text{W cm}^{-1} \text{K}^{-2}$ —representing a 19% increase over the as-deposited counterpart (PF = $20.0 \mu\text{W cm}^{-1} \text{K}^{-2}$). This enhancement is attributed to improved crystallinity, grain growth, and optimized carrier transport due to reduced defect density and better grain boundary connectivity. However, annealing at 300°C and 350°C results in a noticeable decline in the PFs of Bi-Te films compared to their as-prepared counterparts. This suggests that excessive thermal treatment may cause microstructural degradation and phase transformation to Bi₄Te₅ that led to the increased n and reduced S .

Table 1 summarizes the thermoelectric properties of Bi-Te thin films investigated in this study, both before and after annealing, and compares them with relevant results from previous studies. The data clearly show that annealing significantly enhances the thermoelectric performance. For the n-type Bi₂Te₃ films prepared in this work, annealing slightly reduces the electrical resistivity (from $0.80 \text{ m}\Omega\cdot\text{cm}$ to $0.79 \text{ m}\Omega\cdot\text{cm}$) while increasing the absolute value of the Seebeck coefficient (from $-126.9 \mu\text{V/K}$ to $-137.9 \mu\text{V/K}$), resulting in an improved PF from 20.0 to $23.8 \mu\text{W}\cdot\text{cm}^{-1}\text{K}^{-2}$.

Morgan et al. [14] reported pioneering work on n-type Bi-Te thin films fabricated by RF magnetron co-sputtering on flexible polyimide substrates (150 nm thickness), achieving PF = $2.24 \mu\text{W}\cdot\text{cm}^{-1}\cdot\text{K}^{-2}$ after annealing at 300°C. Their work demonstrated successful implementation on flexible substrates

compatible with wearable energy harvesting applications [14]. The significantly lower PF and $|S|$ values ($-30.2 \mu\text{V/K}$ vs. $-137.9 \mu\text{V/K}$ in this work) compared to our rigid-substrate PLD films can be attributed to complementary processing constraints. First, flexible polyimide substrates impose a maximum processing temperature of approximately 300°C due to polymer thermal stability limits, which restricts grain growth and crystallinity enhancement. In contrast, rigid SiO_2/Si (100) substrates used in this study enable systematic optimization of (T_S, T_A) up to 350°C . Second, the thinner films in Ref. [14] (150 nm versus $\geq 600 \text{ nm}$ in this work) prioritize mechanical flexibility rather than maximizing power output. Importantly, both approaches are complementary: Morgan's work establishes scalable and flexible fabrication routes, whereas the present PLD-based study defines performance benchmarks under optimized rigid-substrate conditions. Moreover, PLD and magnetron sputtering offer distinct advantages. PLD typically provides higher plasma kinetic energy, promoting dense and highly textured films with enhanced carrier mobility, albeit limited to centimeter-scale substrates. In contrast, magnetron sputtering supports wafer-scale deposition on both rigid and flexible substrates, making it more suitable for industrial scaling despite generally producing slightly lower-density films.

For PLD-grown Bi_2Te_3 thin films, the optimized high PF of $23.8 \mu\text{W}\cdot\text{cm}^{-1}\cdot\text{K}^{-2}$ for the layered compact-polycrystalline $T_S=T_A=250^\circ\text{C}$ - film in this study exceeds the PF reported for nanoparticle-structured Bi_2Te_3 films ($1.9 \mu\text{W}\cdot\text{cm}^{-1}\cdot\text{K}^{-2}$) [28] and smooth-polycrystalline films ($18.1 \mu\text{W}\cdot\text{cm}^{-1}\cdot\text{K}^{-2}$) [85], and is slightly higher than that of compact-smooth films ($21.2 \mu\text{W}\cdot\text{cm}^{-1}\cdot\text{K}^{-2}$) [86]. Although the PF remains below that of smooth epitaxial Bi_2Te_3 films grown by molecular beam epitaxy (MBE, $27 \mu\text{W}\cdot\text{cm}^{-1}\cdot\text{K}^{-2}$) [87], and approximately half of the exceptionally high PF ($50.6 \mu\text{W}\cdot\text{cm}^{-1}\cdot\text{K}^{-2}$) reported for highly (001)-oriented layered Bi_2Te_3 films deposited at $T_S = 250^\circ\text{C}$ [86], it should be noted that those values were achieved under highly controlled epitaxial or strongly texture-engineered growth conditions.

Compared with alternative fabrication approaches, composite films consisting of carbon nanotubes and Bi_2Te_3 nanowires subjected to pressing and thermal annealing exhibited a resistivity of $4.2 \text{ m}\Omega\cdot\text{cm}$, a Seebeck coefficient of $-175.2 \mu\text{V/K}$, and a PF of $7.4 \mu\text{W}\cdot\text{cm}^{-1}\cdot\text{K}^{-2}$ [37], which remain substantially

lower than the performance achieved in this work. Similarly, optimized Bi_2Te_3 films deposited on SiO_2/Si substrates at 225°C showed a PF of $\sim 3.0 \mu\text{W}\cdot\text{cm}^{-1}\cdot\text{K}^{-2}$ [56], nearly eight times lower than the present result. Notably, X. Wang *et al.* [88] reported a relatively high PF of $21.0 \mu\text{W}\cdot\text{cm}^{-1}\cdot\text{K}^{-2}$ for Bi_2Te_3 thin films prepared by RF magnetron co-sputtering at $T_S = 150^\circ\text{C}$ followed by post-annealing at 300°C , which is comparable but still slightly lower than the optimized value obtained here. Overall, these comparisons indicate that the PLD-grown Bi_2Te_3 thin films developed in this study achieve performance at the upper range of reported polycrystalline systems, approaching epitaxial benchmarks while maintaining practical growth conditions.

For comparison, total thermal conductivity (κ) in high-performance Bi_2Te_3 -based systems has been reported as $\kappa = 1.6 \text{ Wm}^{-1}\text{K}^{-1}$ for bulk hot-pressed $\text{Bi}_2\text{Te}_{2.7}\text{Se}_{0.3}$ ($ZT \approx 0.6$) [80], $0.61\text{--}0.80 \text{ Wm}^{-1}\text{K}^{-1}$ for nanocrystalline $\text{Bi}_2\text{Te}_{3-x}\text{Se}_x$ thin films [89], and $0.46\text{--}0.81 \text{ Wm}^{-1}\text{K}^{-1}$ for sputtered nanocrystalline Bi–Sb–Te films [90]. For PLD-grown films, κ values range from $0.031\text{--}0.296 \text{ Wm}^{-1}\text{K}^{-1}$ in $\text{Bi}_2\text{Te}_3/\text{Sb}_2\text{Te}_3$ superlattice films [91], to approximately $0.8 \text{ Wm}^{-1}\text{K}^{-1}$ ($ZT \approx 0.7$) for $\text{Bi}_2\text{Te}_{2.7}\text{Se}_{0.3}$ films [80], and $0.93\text{--}1.16 \text{ Wm}^{-1}\text{K}^{-1}$ ($ZT = 0.39\text{--}0.65$ at 300 K) for $\text{Bi}_x\text{Sb}_{2-x}\text{Te}_3$ films with grain sizes of $10\text{--}190 \text{ nm}$ [82]. Considering these reported values for both bulk and thin-film Bi_2Te_3 -based materials, a representative $\kappa \approx 1.4 \text{ W}\cdot\text{m}^{-1}\cdot\text{K}^{-1}$ can be reasonably assumed for the Bi_2Te_3 film ($T_S = T_A = 250^\circ\text{C}$) exhibiting the maximum PF of $23.8 \mu\text{W}\cdot\text{cm}^{-1}\cdot\text{K}^{-2}$ in this work. Under this assumption, the estimated ZT at 300 K is approximately 0.51, indicating competitive room-temperature thermoelectric performance among PLD-grown polycrystalline Bi_2Te_3 thin films.

3.3. Magnetotransport property of an optimal thermoelectric Bi_2Te_3 thin film

To investigate the signatures of topological surface states (TSSs) in the Bi_2Te_3 thin films, temperature-dependent magnetoresistance [MR; $\text{MR}(\%) = [R(B) - R(0)] \times 100 / R(0)$] measurement was performed on the optimal thermoelectric Bi_2Te_3 thin film prepared at $T_S = 250^\circ\text{C}$ and $T_A = 250^\circ\text{C}$. Fig. 10(a) shows the MR curves recorded between 2 K and 10 K under a perpendicular magnetic field ($\pm 2.0\text{T}$). At low magnetic fields ($\leq 1.0 \text{ T}$), a clear weak anti-localization (WAL) effect is observed, marked

by a sharp rise in resistance with increasing field; however, this feature gradually weakens as the temperature increases. In topological insulators (TIs), WAL arises from strong spin–orbit coupling in the bulk and the helical spin texture of surface states [43, 46, 92, 93]. The low-field 2D WAL behavior observed here is well described by the Hikami–Larkin–Nagaoka (HLN) model for systems with strong spin–orbit interaction [46, 93], which is

$$\frac{\Delta R_{\square}(B)}{[R_{\square}(0)]^2} = -\alpha \frac{e^2}{2\pi^2\hbar} \left[\Psi\left(\frac{1}{2} + \frac{B_{\phi}}{B}\right) - \ln\left(\frac{B_{\phi}}{B}\right) \right] \quad (4)$$

where R_{\square} denotes the sheet resistance, $\Delta R_{\square} = R_{\square}(B) - R_{\square}(0)$, $\Psi(x)$ is the digamma function, $B_{\phi} = \hbar/(4eL_{\phi}^2)$ is the characteristic magnetic field related to the phase coherence length L_{ϕ} . The parameter α reflects the number of coherent conduction channels, where $\alpha = -1/2$ corresponds to a single 2D transport channel, and $\alpha = -1$ represents two independent channels with comparable L_{ϕ} values in 3D topological insulators [46, 93, 94]. The MR results within $B \pm 1.0$ T fit well with Eq. (4) (green curves in Fig. 10a), enabling extraction of the temperature-dependent L_{ϕ} and α (Fig. 10b). At 2 K, L_{ϕ} is 186.2 nm – smaller than the reported ~ 331 nm for a 50-nm-thick Bi_2Te_3 film [92] and ~ 280 nm for Bi_2Te_3 microflakes [94]. As temperature increases, L_{ϕ} steadily declines, following a power-law dependence of $L_{\phi} \sim T^{-0.88}$. Theoretically, the coherence length follows a power-law dependence of $L_{\phi} \sim T^{-0.5}$ for dominant e–e scattering in 2D weakly disordered systems, while in 3D systems with dominant electron–electron and electron–phonon scatterings, it scales as $L_{\phi} \sim T^{-0.75}$. The observed $L_{\phi} \sim T^{-0.88}$ suggests the coexistence of TSSs and dominant bulk states with strong dephasing effects.

Figure 10(b) shows the temperature-dependent trend of $-\alpha(T)$, where $-\alpha$ remains in the range of 0.45–0.48 at low temperatures (2–5 K), then increases to 0.59 at 7 K and 0.67 at 10 K. This trend indicates that the film exhibits a single coherent transport channel in the low-temperature regime, while the charge transport channels gradually decouple with increasing temperature. This decoupling occurs because thermal energy disrupts phase coherence, leading to the separation of previously entangled transport

pathway. The observation of 2D WAL behavior suggests the presence of entangled phase-coherent channels involving both a 2D TSS and a 3D bulk state in the studied Bi₂Te₃ thin films.

3.4. Ultrafast dynamics in the optimized thermoelectric Bi₂Te₃ thin film

Figure 11(a) displays the transient reflectivity change ($\Delta R/R$) spectrum of the optimized TE Bi₂Te₃ thin film, measured at a pump fluence of 0.2 mJ/cm². A sharp initial rise in the $\Delta R/R$ signal reflects the rapid excitation of electrons from the valence band to the conduction band induced by the ultrafast laser pulse. The observed dynamics in Fig. 11(a) were analyzed by fitting the data using Equation (5).

$$\frac{\Delta R}{R} = A_1 \exp(-t / \tau_1) + A_2 \exp(-t / \tau_2) \quad (5)$$

where A_1, A_2 and τ_1, τ_2 are the amplitudes and the relaxation times of hot carriers via various processes, respectively.

The fitting of the $\Delta R/R$ spectra, as shown in the inset of Fig. 11(a), yielded two characteristic relaxation times: $\tau_1 = 0.9 \pm 0.1$ ps and $\tau_2 = 218 \pm 17.2$ ps. The faster component, τ_1 , corresponds to the relaxation of hot carriers, predominantly governed by electron–electron scattering and electron–phonon interactions. This timescale is consistent with previously reported values for bismuth chalcogenide systems, such as ~ 1.0 ps in Bi_{1.5}Sb_{0.5}Te_{1.8}Se_{1.2} single crystals [95], ~ 2 ps in Bi_{2-x}Sb_xSe₃ [96], and ~ 2.3 ps in Bi₂Se₃ single crystals [97]. The slower relaxation time, τ_2 , likely arises from photocarrier recombination processes and aligns reasonably with the reported value of 111 ps for Bi₂Te₃ thin films deposited by PLD [50].

By subtracting the fitted curve from the pump–probe reflectivity spectrum, both fast and slow oscillatory components were isolated (Figs. 11b,c). These signals were then analyzed using the Fast Fourier Transform (FFT) to identify the corresponding phonon frequencies. A prominent coherent phonon mode was detected at 1.87 THz (Fig. 11d), consistent with the reported 1.84–1.85 THz longitudinal optical phonon mode in Bi₂Te₃ thin films [50, 98], which is attributed to the excitation of

the A_{1g}^1 longitudinal optical phonon mode in Bi_2Te_3 [99]. Additionally, a second frequency component at 37.3 GHz was observed (Fig. 11e), which can be reasonably attributed to a bulk acoustic phonon mode of Bi_2Te_3 . This value aligns with previous findings in $\text{Bi}_2\text{Se}_2\text{Te}$ thin films (~33.0 GHz) [51, 52] and closely matches acoustic phonon frequencies in other semiconducting materials, such as (001) ZnTe (41 GHz) [100], (100) GaAs (44 GHz) [101], and SnS (39.06 GHz along the zigzag direction) [102].

4. Conclusion

This work presents a comprehensive investigation into the fabrication and TE optimization of n-type Bi_2Te_3 thin films grown by PLD on SiO_2/Si substrates. By tuning the T_S from 25°C to 350 °C under 220 mTorr helium, we demonstrated clear correlations between growth conditions, morphology, crystal orientation, composition, and TE properties. The film morphology evolved from nanoparticles to layered hexagonal platelets, while the preferred orientation shifted from (015) to highly (001)-oriented textures. Near-stoichiometric Bi_2Te_3 films formed at 250–300°C exhibited reduced carrier concentration and significantly improved mobility (up to 81.2 $\text{cm}^2/\text{V}\cdot\text{s}$), resulting in an enhanced PF of 20.0 $\mu\text{W}\cdot\text{cm}^{-1}\cdot\text{K}^{-2}$. To further boost performance, in-situ annealing at T_A of 200–350°C was applied to films grown at 200, 250, and 300°C. This dual tuning of T_S and T_A revealed a processing window for optimal TE power factor, achieving a peak PF of 23.8 $\mu\text{W}\cdot\text{cm}^{-1}\cdot\text{K}^{-2}$ for the film deposited at 250°C and annealed at 250°C—a 19% enhancement. Additionally, low-temperature magnetotransport measurements on the optimized TE film revealed two-dimensional weak antilocalization, indicating potential contributions from topological surface states. Ultrafast pump–probe spectroscopy confirmed coherent phonon dynamics, with an optical phonon at 1.87 THz (A_{1g}^1 mode) and an acoustic phonon at 37.3 GHz. Overall, this study underscores the importance of precise growth and annealing temperatures in tailoring both TE and quantum transport properties of Bi_2Te_3 thin films, offering valuable guidance for the development of high-performance, multifunctional thermoelectric materials.

Le Thi Cam Tuyen: Data curation, Investigation, Formal Analysis, Writing – original draft. **Phuoc Huu Le:** Conceptualization, Methodology, Investigation, Formal Analysis, Writing – original draft, Project administration. **Bih-Show Lou, Jyh-Wei Lee, Chien-Neng Liao:** Resources, Validation, Review & editing. **Ngo Ngoc Uyen:** Investigation, Writing – Review & editing. **Chih-Wei Luo:** Resources, Validation, Writing – Review & editing, Supervision. **Jiunn-Yuan Lin:** Resources of PLD and PPMS facilities.

Declaration of competing interest

The authors declare that they have no known competing financial interests or personal relationships that could have appeared to influence the work reported in this paper.

Acknowledgments

This research was funded by the National Science and Technology Council of Taiwan under grant number NSTC 113-2222-E-131-003- and [NSTC 114-2637-E-131-004-](#) (P.H. Le). An author (N.N. Uyen) acknowledges the support of Can Tho University of Medicine and Pharmacy, Vietnam in facilitating this study.

References

- [1] Venkatasubramanian R, Siivola E, Colpitts T, et al. Thin-film thermoelectric devices with high room-temperature figures of merit. *Nature*. 2001;413:597-602. doi: 10.1038/35098012
- [2] Snyder GJ, Toberer ES. Complex thermoelectric materials. *Nature Materials*. 2008;7:105-114. doi: 10.1038/nmat2090
- [3] Ao D, Li F, Chen Y, et al. CoSb₃-Based Thin-Film Thermoelectric Devices with High Performance Via Electrode Optimization. *ACS Applied Energy Materials*. 2021;4:5265-5273. doi: 10.1021/acsaem.1c00795
- [4] Yang F, Zheng S, Wang H, et al. A thin film thermoelectric device fabricated by a self-aligned shadow mask method. *Journal of Micromechanics and Microengineering*. 2017;27:055005. doi: 10.1088/1361-6439/aa64a3
- [5] Snyder GJ, Lim JR, Huang C-K, et al. Thermoelectric microdevice fabricated by a MEMS-like electrochemical process. *Nature Materials*. 2003;2:528-531. doi: 10.1038/nmat943
- [6] Corbett S, Gautam D, Lal S, et al. Electrodeposited Thin-Film Micro-Thermoelectric Coolers with Extreme Heat Flux Handling and Microsecond Time Response. *ACS Applied Materials & Interfaces*. 2021;13:1773-82. doi: 10.1021/acsaami.0c16614
- [7] Ming T, Chen S, Yan Y, et al. The simulated cooling performance of a thin-film thermoelectric cooler with coupled-thermoelements connected in parallel. *Heliyon*. 2022;8:e10025. doi: 10.1016/j.heliyon.2022.e10025
- [8] Mehdizadeh Dehkordi A, Zebajadi M, He J, et al. Thermoelectric power factor: Enhancement mechanisms and strategies for higher performance thermoelectric materials. *Materials Science and Engineering: R: Reports*. 2015;97:1-22. doi: 10.1016/j.mser.2015.08.001
- [9] Tadano T, Gohda Y, Tsuneyuki S. Impact of Rattlers on Thermal Conductivity of a Thermoelectric Clathrate: A First-Principles Study. *Physical Review Letters*. 2015;114:095501. doi: 10.1103/PhysRevLett.114.095501
- [10] Mascali G. Thermal conductivity reduction by embedding nanoparticles. *Journal of Computational Electronics*. 2017;16:180-9. doi: 10.1007/s10825-016-0934-y
- [11] Pichanusakorn P, Bandaru P. Nanostructured thermoelectrics. *Materials Science and Engineering: R: Reports*. 2010;67:19-63. doi: 10.1016/j.mser.2009.10.001
- [12] Poudel B, Hao Q, Ma Y, et al. High-Thermoelectric Performance of Nanostructured Bismuth Antimony Telluride Bulk Alloys. *Science*. 2008;320:634-8. doi: 10.1126/science.1156446
- [13] Zhou J, Zhu H, Liu T-H, et al. Large thermoelectric power factor from crystal symmetry-protected non-bonding orbital in half-Heuslers. *Nature Communications*. 2018;9:1721. doi: 10.1038/s41467-018-03866-w
- [14] Morgan KA, Zeimpekis I, Feng Z, et al. Enhancing thermoelectric properties of bismuth telluride and germanium telluride thin films for wearable energy harvesting. *Thin Solid Films*. 2022;741:139015. doi: 10.1016/j.tsf.2021.139015
- [15] Saberi Y, Sajjadi SA. A comprehensive review on the effects of doping process on the thermoelectric properties of Bi₂Te₃ based alloys. *Journal of Alloys and Compounds*. 2022;904:163918. doi: 10.1016/j.jallcom.2022.163918
- [16] Goncalves LM, Couto C, Alpuim P, et al. Optimization of thermoelectric properties on Bi₂Te₃ thin films deposited by thermal co-evaporation. *Thin Solid Films*. 2010;518:2816-21. doi: 10.1016/j.tsf.2009.08.038
- [17] Samanta M, Pal K, Waghmare UV, et al. Intrinsically Low Thermal Conductivity and High Carrier Mobility in Dual Topological Quantum Material, n-Type BiTe. *Angew Chem Int Ed Engl*. 2020;59:4822-9. doi: 10.1002/anie.202000343
- [18] Liebl J, Neugebauer S, Eder A, et al. The thermoelectric generator from BMW is making use of waste heat. *MTZ worldwide*. 2009;70:4-11. doi: 10.1007/BF03226939
- [19] Zaferani SH, Sams MW, Ghomashchi R, et al. Thermoelectric coolers as thermal management systems for medical applications: Design, optimization, and advancement. *Nano Energy*. 2021;90:106572. doi: 10.1016/j.nanoen.2021.106572
- [20] Hu B, Shi X-L, Zou J, et al. Thermoelectrics for medical applications: Progress, challenges, and perspectives. *Chemical Engineering Journal*. 2022;437:135268. doi: 10.1016/j.cej.2022.135268
- [21] Kong D, Zhu W, Guo Z, et al. High-performance flexible Bi₂Te₃ films based wearable thermoelectric generator for energy harvesting. *Energy*. 2019;175:292-299. doi: 10.1016/j.energy.2019.03.060
- [22] Sharma PA, Sharma ALL, Medlin DL, et al. Low phonon thermal conductivity of layered (Bi₂)_m-(Bi₂Te₃)_n thermoelectric alloys. *Physical Review B*. 2011;83:235209. doi: 10.1103/PhysRevB.83.235209
- [23] Tan M, Deng Y, Wang Y, et al. Improved performance of thermoelectric micro-device by integrating a layered Bi₂Te₃ film. *Thin Solid Films*. 2013;548:526-32. doi: 10.1016/j.tsf.2013.08.091
- [24] Lu Y, Zhou Y, Wang W, et al. Staggered-layer-boosted flexible Bi₂Te₃ films with high thermoelectric performance. *Nature Nanotechnology*. 2023;18:1281-1288. doi: 10.1038/s41565-023-01457-5
- [25] Newbrook DW, Richards SP, Greenacre VK, et al. Improved thermoelectric performance of Bi₂Se₃ alloyed Bi₂Te₃ thin films via low pressure chemical vapour deposition. *Journal of Alloys and Compounds*. 2020;848:156523. doi: 10.1016/j.jallcom.2020.156523

- [26] Lu F, Liu S, Dai M, et al. Spin-coating co-reduction method to prepare Bi₂Te₃ films and its tunable thermoelectric properties. *Journal of Alloys and Compounds*. 2025;1018:179183. doi: 10.1016/j.jallcom.2025.179183
- [27] Le PH, Liao C-N, Luo CW, et al. Thermoelectric properties of nanostructured bismuth–telluride thin films grown using pulsed laser deposition. *Journal of Alloys and Compounds*. 2014;615:546-552. doi: 10.1016/j.jallcom.2014.07.018
- [28] Chang H-C, Chen C-H. Self-assembled bismuth telluride films with well-aligned zero- to three-dimensional nanoblocks for thermoelectric applications. *CrystEngComm*. 2011;13:5956-5962. doi: 10.1039/C1CE05350G
- [29] Chen T-H, Lin P-Y, Chang H-C, et al. Enhanced thermoelectricity of three-dimensionally mesostructured Bi_xSb_{2-x}Te₃ nanoassemblies: from micro-scaled open gaps to isolated sealed mesopores. *Nanoscale*. 2017;9:3283-3292. doi: 10.1039/C7NR00132K
- [30] Tuyen LTC, Le PH, Luo CW, et al. Thermoelectric properties of nanocrystalline Bi₃Se₂Te thin films grown using pulsed laser deposition. *Journal of Alloys and Compounds*. 2016;673:107-114. doi: 10.1016/j.jallcom.2016.03.006
- [31] Schou J. Physical aspects of the pulsed laser deposition technique: The stoichiometric transfer of material from target to film. *Applied Surface Science*. 2009;255:5191-5198. doi: 10.1016/j.apsusc.2008.10.101
- [32] Shepelin NA, Tehrani ZP, Ohannessian N, et al. A practical guide to pulsed laser deposition. *Chemical Society Reviews*. 2023;52:2294-321. doi: 10.1039/D2CS00938B
- [33] Haider AJ, Alawsi T, Haider MJ, et al. A comprehensive review on pulsed laser deposition technique to effective nanostructure production: trends and challenges. *Optical and Quantum Electronics*. 2022;54:488. doi: 10.1007/s11082-022-03786-6
- [34] Le PH, Liao C-N, Luo CW, et al. Thermoelectric properties of bismuth-selenide films with controlled morphology and texture grown using pulsed laser deposition. *Applied Surface Science*. 2013;285:657-663. doi: 10.1016/j.apsusc.2013.08.107
- [35] Martin J, Wang L, Chen L, et al. Enhanced Seebeck coefficient through energy-barrier scattering in PbTe nanocomposites. *Physical Review B*. 2009;79:115311. doi: 10.1103/PhysRevB.79.115311
- [36] Bailini A, Donati F, Zamboni M, et al. Pulsed laser deposition of Bi₂Te₃ thermoelectric films. *Applied Surface Science*. 2007;254:1249-1254. doi: 10.1016/j.apsusc.2007.09.039
- [37] An H, Pusko M, Chun D, et al. In-situ synthesis of flexible hybrid composite films for improved thermoelectric performance. *Chemical Engineering Journal*. 2019;357:547-558. doi: 10.1016/j.cej.2018.09.200
- [38] Singh S, Singh J, Kaushal J, et al. Effects of annealing on the thermoelectric properties of nanocrystalline Bi_{1.2}Sb_{0.8}Te₃ thin films prepared by thermal evaporation. *Applied Physics A*. 2019;125:144. doi: 10.1007/s00339-019-2420-4
- [39] Moore JE. The birth of topological insulators. *Nature*. 2010;464:194-198. doi: 10.1038/nature08916
- [40] Hsieh D, Xia Y, Qian D, et al. Observation of Time-Reversal-Protected Single-Dirac-Cone Topological-Insulator States in Bi₂Te₃ and Sb₂Te₃. *Physical Review Letters*. 2009;103:146401. doi: 10.1103/PhysRevLett.103.146401
- [41] Xu L, Zheng Y, Zheng J-C. Thermoelectric transport properties of PbTe under pressure. *Physical Review B*. 2010;82:195102. doi: 10.1103/PhysRevB.82.195102
- [42] Zhang SX, McDonald RD, Shekhter A, et al. Magneto-resistance up to 60 Tesla in topological insulator Bi₂Te₃ thin films. *Applied Physics Letters*. 2012;101:202403. doi: 10.1063/1.4766739
- [43] Cha JJ, Kong D, Hong S-S, et al. Weak Antilocalization in Bi₂(Se_xTe_{1-x})₃ Nanoribbons and Nanoplates. *Nano Letters*. 2012;12:1107-11. doi: 10.1021/nl300018j
- [44] Le PH, Liu P-T, Luo CW, et al. Thickness-dependent magnetotransport properties and terahertz response of topological insulator Bi₂Te₃ thin films. *Journal of Alloys and Compounds*. 2017;692:972-979. doi: 10.1016/j.jallcom.2016.09.109
- [45] Wang W, Li L, Zou W, et al. Intrinsic Topological Insulator Bi_{1.5}Sb_{0.5}Te_{3-x}Se_x Thin Crystals. *Scientific Reports*. 2015;5:7931. doi: 10.1038/srep07931
- [46] Le PH, Tuyen LTC, Quyen NN, et al. Thickness-dependent magnetotransport and ultrafast dynamic properties of epitaxial Bi₂Se₃/InP(111) thin films grown using pulsed laser deposition. *Chinese Journal of Physics*. 2024;91:857-866. doi: 10.1016/j.cjph.2024.08.030
- [47] Braun L, Mussler G, Hruban A, et al. Ultrafast photocurrents at the surface of the three-dimensional topological insulator Bi₂Se₃. *Nature Communications*. 2016;7:13259. doi: 10.1038/ncomms13259
- [48] Glinka YD, Babakiray S, Johnson TA, et al. Ultrafast carrier dynamics in thin-films of the topological insulator Bi₂Se₃. *Applied Physics Letters*. 2013;103:151903. doi: 10.1063/1.4824821
- [49] Weis M, Balin K, Rapacz R, et al. Ultrafast light-induced coherent optical and acoustic phonons in few quintuple layers of the topological insulator Bi₂Te₃. *Physical Review B*. 2015;92:014301. doi: 10.1103/PhysRevB.92.014301
- [50] Xu Z, Yao J, Yang G, et al. Ultrafast dynamics of photoexcited carriers and coherent phonons in ultrathin Bi₂Te₃ thermoelectric films. *Science China Physics, Mechanics & Astronomy*. 2021;65:217312. doi: 10.1007/s11433-021-1795-5
- [51] Mukhopadhyay U, Chaudhuri D, Sarkar J, et al. Surface optical and bulk acoustic phonons in the topological insulator, Bi₂Se₂Te. *Applied Physics Letters*. 2015;106:241106. doi: 10.1063/1.4922641

- [52] Le PH, Tuyen LTC, Quyen NN, et al. Weak antilocalization and gigahertz acoustic phonons in $\text{Bi}_2\text{Se}_2\text{Te}$ and $\text{Bi}_3\text{Se}_2\text{Te}$ -dominated thin films grown using pulsed laser deposition. *Thin Solid Films*. 2024;791:140241. doi: 10.1016/j.tsf.2024.140241
- [53] William Nuttall RC, Bartek Glowacki. *The Future of Helium as a Natural Resource*. 1st ed: Routledge, Taylor & Francis Group; 2012.
- [54] Testardi LR, McConnell GK. Measurement of the Seebeck Coefficient with Small Temperature Differences. *Review of Scientific Instruments*. 1961;32:1067-1068. doi: 10.1063/1.1717624
- [55] Kuznetsov PI, Yapaskurt VO, Shchamkhalova BS, et al. Growth of Bi_2Te_3 films and other phases of Bi-Te system by MOVPE. *Journal of Crystal Growth*. 2016;455:122-128. doi: 10.1016/j.jcrysgro.2016.09.055
- [56] Kim D-H, Byon E, Lee G-H, et al. Effect of deposition temperature on the structural and thermoelectric properties of bismuth telluride thin films grown by co-sputtering. *Thin Solid Films*. 2006;510:148-53. doi: 10.1016/j.tsf.2005.12.306
- [57] Faraji LS, Singh RP, Allahkarami M. Pulsed laser deposition of bismuth telluride thin film and annealing effects. *The European Physical Journal Applied Physics*. 2009;46:20501. doi: 10.1051/epjap/2009053
- [58] Sahu BP, Sharma P, Yadav SK, et al. Influence of strain and point defects on the electronic structure and related properties of (111)NiO epitaxial films. *Journal of Physics D: Applied Physics*. 2025;58:085302. doi: 10.1088/1361-6463/ad98a4
- [59] Mzerd A, Sayah D, Brun G, et al. Crystal growth and sticking coefficient of Bi_2Te_3 thin films on Si(111) substrate. *Journal of Materials Science Letters*. 1995;14:194-197. doi: 10.1007/BF00318254
- [60] Karabacak T, Singh JP, Zhao YP, et al. Scaling during shadowing growth of isolated nanocolumns. *Physical Review B*. 2003;68:125408. doi: 10.1103/PhysRevB.68.125408
- [61] Soni A, Yanyuan Z, Ligen Y, et al. Enhanced thermoelectric properties of solution grown $\text{Bi}_2\text{Te}_{(3-x)}\text{Se}_{(x)}$ nanoplatelet composites. *Nano Lett*. 2012;12:1203-1209. doi: 10.1021/nl2034859
- [62] Bando H, Koizumi K, Oikawa Y, et al. The time-dependent process of oxidation of the surface of Bi_2Te_3 studied by X-ray photoelectron spectroscopy. *Journal of Physics: Condensed Matter*. 2000;12:5607. doi: 10.1088/0953-8984/12/26/307
- [63] Fu J, Song S, Zhang X, et al. Bi_2Te_3 nanoplates and nanoflowers: Synthesized by hydrothermal process and their enhanced thermoelectric properties. *CrystEngComm*. 2012;14:2159. doi: 10.1039/c2ce06348d
- [64] Cicvarić K, Meng L, Newbrook DW, et al. Thermoelectric Properties of Bismuth Telluride Thin Films Electrodeposited from a Nonaqueous Solution. *ACS Omega*. 2020;5:14679-14688. doi: 10.1021/acsomega.0c01284
- [65] Liu S-Q, Liu W-D, Lyu W, et al. Defect Engineering in van der Waals Layer-Structured Bi_2Te_3 -Based Materials. *cMat*. 2025;2:e70009. doi: 10.1002/cmt2.70009
- [66] Hashibon A, Elsässer C. First-principles density functional theory study of native point defects in Bi_2Te_3 . *Physical Review B*. 2011;84:144117. doi: 10.1103/PhysRevB.84.144117
- [67] Wang G, Zhu XG, Sun YY, et al. Topological insulator thin films of Bi_2Te_3 with controlled electronic structure. *Adv Mater*. 2011;23:2929-2932. doi: 10.1002/adma.201100678
- [68] Zhu T, Hu L, Zhao X, et al. New Insights into Intrinsic Point Defects in V_2VI_3 Thermoelectric Materials. *Advanced Science*. 2016;3:1600004. doi: 10.1002/advs.201600004
- [69] Xu Z, Wu H, Zhu T, et al. Attaining high mid-temperature performance in $(\text{Bi,Sb})_2\text{Te}_3$ thermoelectric materials via synergistic optimization. *NPG Asia Materials*. 2016;8:e302-e. doi: 10.1038/am.2016.134
- [70] Siegal MP, Podkaminer J, Lima-Sharma AL, et al. Correlating thermoelectric $(\text{Bi,Sb})_2\text{Te}_3$ film electric transport properties with microstructure. *Journal of Applied Physics*. 2019;125:175107. doi: 10.1063/1.5089647
- [71] Mukherjee B, Tarachand, Lakhani A, et al. Impact of Copper Intercalation on Thermoelectric Properties in Polyol Method-Prepared $\text{Cu}_x\text{Bi}_2\text{Se}_3$, $x = 0, 0.05, 0.10$, and 0.15 Nanosheets. *ACS Applied Energy Materials*. 2023;6:8572-80. doi: 10.1021/acsaem.3c01465
- [72] Tang X, Li Z, Liu W, et al. A comprehensive review on Bi_2Te_3 -based thin films: Thermoelectrics and beyond. *Interdisciplinary Materials*. 2022;1:88-115. doi: 10.1002/idm2.12009
- [73] Novitskii A, Mori T. Revisiting Pisarenko's formula: Effective mass estimation, thermopower–conductivity relation, and maximum power factor prediction. *Materials Today Physics*. 2025;58:101845. doi: 10.1016/j.mtphys.2025.101845
- [74] Rogacheva EI, Budnik AV, Sipatov AY, et al. Thickness dependent quantum oscillations of transport properties in topological insulator Bi_2Te_3 thin films. *Applied Physics Letters*. 2015;106:053103. doi: 10.1063/1.4907319
- [75] Parashchuk T, Kostyuk O, Nykyruy L, et al. High thermoelectric performance of p-type $\text{Bi}_{0.5}\text{Sb}_{1.5}\text{Te}_3$ films on flexible substrate. *Materials Chemistry and Physics*. 2020;253:123427. doi: 10.1016/j.matchemphys.2020.123427
- [76] Shigetomi S, Mori S. Electrical Properties of Bi_2Te_3 . *J Phys Soc Jpn*. 1956;11:915-9. doi: 10.1143/JPSJ.11.915
- [77] Witting IT, Chasapis TC, Ricci F, et al. The Thermoelectric Properties of Bismuth Telluride. *Advanced Electronic Materials*. 2019;5:1800904. doi: 10.1002/aelm.201800904

- [78] Mao D, Yang J, Han M, et al. Homo-layer flexible Bi_2Te_3 -based films with high thermoelectric performance. *Science Advances*. 11:eadz1019. doi: 10.1126/sciadv.adz1019
- [79] Ouyang Y, Zhang M, Zhan F, et al. Intrinsically large effective mass and multi-valley band characteristics of n-type $\text{Bi}_2\text{Bi}_2\text{Te}_3$ superlattice-like films. *Journal of Materiomics*. 2024;10:716-724. doi: 10.1016/j.jmat.2023.11.010
- [80] Takashiri M, Takiishi M, Tanaka S, et al. Thermoelectric properties of n-type nanocrystalline bismuth-telluride-based thin films deposited by flash evaporation. *Journal of Applied Physics*. 2007;101:074301. doi: 10.1063/1.2717867
- [81] Cho S, Kim Y, DiVenere A, et al. Antisite defects of Bi_2Te_3 thin films. *Applied Physics Letters*. 1999;75:1401-3. doi: 10.1063/1.124707
- [82] Chang HC, Chen CH, Kuo YK. Great enhancements in the thermoelectric power factor of BiSbTe nanostructured films with well-ordered interfaces. *Nanoscale*. 2013;5:7017-7025. doi: 10.1039/c3nr01499a
- [83] Fan L, Tang J, Wu L, et al. Rapid growth of high-performance Bi_2Te_3 thin films by laser annealing at room temperature. *Applied Surface Science*. 2023;639:158164. doi: 10.1016/j.apsusc.2023.158164
- [84] Lin S-S, Liao C-N. Effect of ball milling and post treatment on crystal defects and transport properties of $\text{Bi}_2(\text{Se},\text{Te})_3$ compounds. *Journal of Applied Physics*. 2011;110:doi: 10.1063/1.3658256
- [85] Sun R, Guo R, Yu X, et al. Brushy C-Decorated BiTe -Based Thermoelectric Film for Efficient Photodetection and Photoimaging. *ACS Appl Mater Interfaces*. 2024;16:45307-18. doi: 10.1021/acsami.4c07979
- [86] Li Bassi A, Bailini A, Casari CS, et al. Thermoelectric properties of Bi-Te films with controlled structure and morphology. *Journal of Applied Physics*. 2009;105:124307. doi: 10.1063/1.3147870
- [87] Peranio N, Eibl O, Nurnus J. Structural and thermoelectric properties of epitaxially grown Bi_2Te_3 thin films and superlattices. *Journal of Applied Physics*. 2006;100:114306. doi: 10.1063/1.2375016
- [88] Wang X, He H, Wang N, et al. Effects of annealing temperature on thermoelectric properties of Bi_2Te_3 films prepared by co-sputtering. *Applied Surface Science*. 2013;276:539-542. doi: 10.1016/j.apsusc.2013.03.130
- [89] Takashiri M, Miyazaki K, Tanaka S, et al. Effect of grain size on thermoelectric properties of n-type nanocrystalline bismuth-telluride based thin films. *Journal of Applied Physics*. 2008;104:084302. doi: 10.1063/1.2990774
- [90] Liao C-N, Wang Y-C, Chu H-S. Thermal transport properties of nanocrystalline Bi-Sb-Te thin films prepared by sputter deposition. *Journal of Applied Physics*. 2008;104:104312. doi: 10.1063/1.3026728
- [91] Walachová J, Zeipl R, Zelinka J, et al. High room-temperature figure of merit of thin layers prepared by laser ablation from Bi_2Te_3 target. *Appl Phys Lett* 2005;87:081902 doi: 10.1063/1.2001755
- [92] He H-T, Wang G, Zhang T, et al. Impurity Effect on Weak Antilocalization in the Topological Insulator Bi_2Te_3 . *Physical Review Letters*. 2011;106:166805. doi: 10.1103/PhysRevLett.106.166805
- [93] Hikami S, Larkin AI, Nagaoka Y. Spin-Orbit Interaction and Magnetoresistance in the Two Dimensional Random System. *Progress of Theoretical Physics*. 1980;63:707-10. doi: 10.1143/PTP.63.707
- [94] Chiu S-P, Lin J-J. Weak antilocalization in topological insulator Bi_2Te_3 microflakes. *Physical Review B*. 2013;87:035122. doi: 10.1103/PhysRevB.87.035122
- [95] Cheng L, La-o-vorakiat C, Tang CS, et al. Temperature-dependent ultrafast carrier and phonon dynamics of topological insulator $\text{Bi}_{1.5}\text{Sb}_{0.5}\text{Te}_{1.8}\text{Se}_{1.2}$. *Applied Physics Letters*. 2014;104:211906. doi: 10.1063/1.4879831
- [96] Gross AL, Hou Y, Rossi A, et al. Nanosecond dynamics in intrinsic topological insulator $\text{Bi}_{2-x}\text{Sb}_x\text{Se}_3$ revealed by time-resolved optical reflectivity. *Physical Review B*. 2021;103:L020301. doi: 10.1103/PhysRevB.103.L020301
- [97] Qi J, Chen X, Yu W, et al. Ultrafast carrier and phonon dynamics in Bi_2Se_3 crystals. *Applied Physics Letters*. 2010;97:182102. doi: 10.1063/1.3513826
- [98] Wu AQ, Xu X, Venkatasubramanian R. Ultrafast dynamics of photoexcited coherent phonon in Bi_2Te_3 thin films. *Applied Physics Letters*. 2008;92:011108. doi: 10.1063/1.2829604
- [99] Richter W, Becker CR. A Raman and far-infrared investigation of phonons in the rhombohedral $\text{V}_2\text{-VI}_3$ compounds Bi_2Te_3 , Bi_2Se_3 , Sb_2Te_3 and $\text{Bi}_2(\text{Te}_{1-x}\text{Se}_x)_3$ ($0 < x < 1$), $(\text{Bi}_{1-y}\text{Sb}_y)_2\text{Te}_3$ ($0 < y < 1$). *physica status solidi (b)*. 1977;84:619-628. doi: 10.1002/pssb.2220840226
- [100] Feng DH, Pan XQ, Li X, et al. Coherent acoustic phonon generation and detection by femtosecond laser pulses in ZnTe single crystals. *Journal of Applied Physics*. 2013;114:093513. doi: 10.1063/1.4820518
- [101] Han X, Wang M, Zhao W, et al. Gigahertz coherent longitudinal acoustic phonons in GaAs Single crystals with different orientations. *Optics Communications*. 2020;461:125257. doi: 10.1016/j.optcom.2020.125257
- [102] Quyen NN, Hong T-J, Hsu CE, et al. Nematic electron and phonon dynamics in SnS crystals. *Applied Physics Letters*. 2022;121:172105. doi: 10.1063/5.0099486

Table 1. Optimized thermoelectric properties of Bi₂Te₃-based thin films with and without annealing, compared with previously reported studies.

Material	Method	Conditions	ρ (m Ω ·cm)	S (μ V/K)	Power factor (μ Wcm ⁻¹ K ⁻²)	Ref
n-Bi ₂ Te ₃	PLD	As-deposited, $T_S=250^\circ\text{C}$	0.80	-126.9	20.0	This work
n-Bi ₂ Te ₃	PLD	$T_S = T_A = 250^\circ\text{C}$	0.79	-137.9	23.8	This work
n-BiTe	Sputtering	As-deposited, $T_S = \text{room}$ temperature	0.77	-32.0	1.33	[14]
n-BiTe	Sputtering	$T_A = 300^\circ\text{C}$, 1h	0.41	-30.0	2.24	[14]
n-Bi ₂ Te ₃	Sputtering	$T_S = 350^\circ\text{C}$	1.97	-102.0	1.49	[23]
n-Bi ₂ Te ₃	PLD	$T_A = 300^\circ\text{C}$	---	-188.6	18.1	[85]
n-Bi ₂ Te ₃	PLD	$T_S = 250^\circ\text{C}$	0.68	-186.0	50.6	[86]
n-Bi ₂ Te ₃	PLD	$T_S = 350^\circ\text{C}$	1.88	-170.0	21.2	[86]
n-Bi ₂ Te ₃	PLD	$T_S = 300^\circ\text{C}$	4.35	-91.0	1.9	[28]
n-Bi ₂ Te ₃	MBE	$T_S = 280^\circ\text{C}$	1.49	-201.0	27.0	[87]
n-Bi ₂ Te ₃	Thermal evaporation	CO ₂ laser annealing at 6.6 mJ/cm ²	3.5	-165.4	8.2	[83]
CNT/Bi ₂ Te ₃	Solution method	$T_A = 300^\circ\text{C}$, 2 h, Ar gas flow	4.2	-175.2	7.4	[37]
n-Bi ₂ Te ₃	Co-sputtering	$T_S = 225^\circ\text{C}$	10.5	-55.0	~3.0	[56]
n-Bi ₂ Te ₃	Co-sputtering	$T_S = \text{room-temperature};$ $T_A = 300^\circ\text{C}$	0.19	-242	21.0	[88]

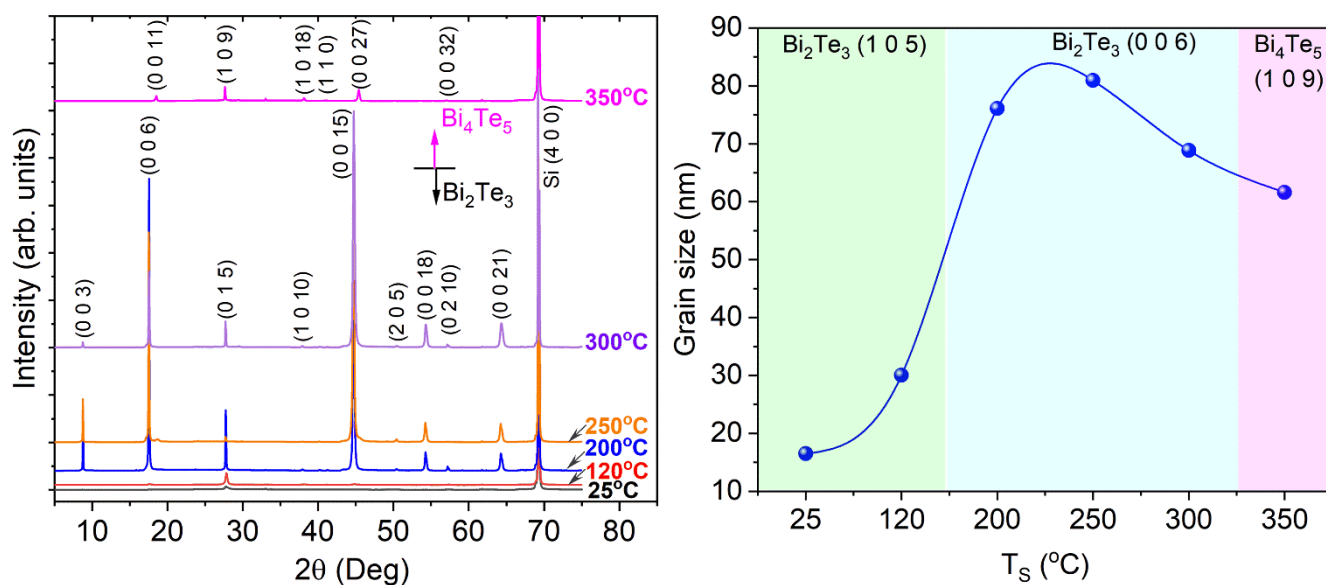


Figure 1. (a) XRD patterns of Bi-Te thin films deposited at various substrate temperature (T_s) ranging from 25 to 350°C. (b) Grain size of the films estimated by Scherer equation.

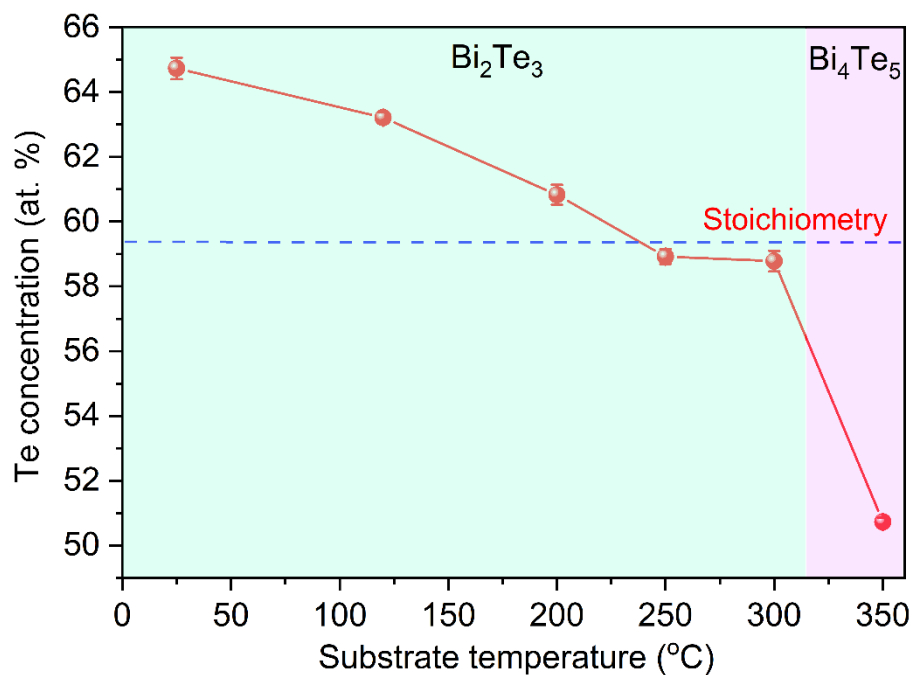


Figure 2. Variation of Te concentration as a function of substrate temperature.

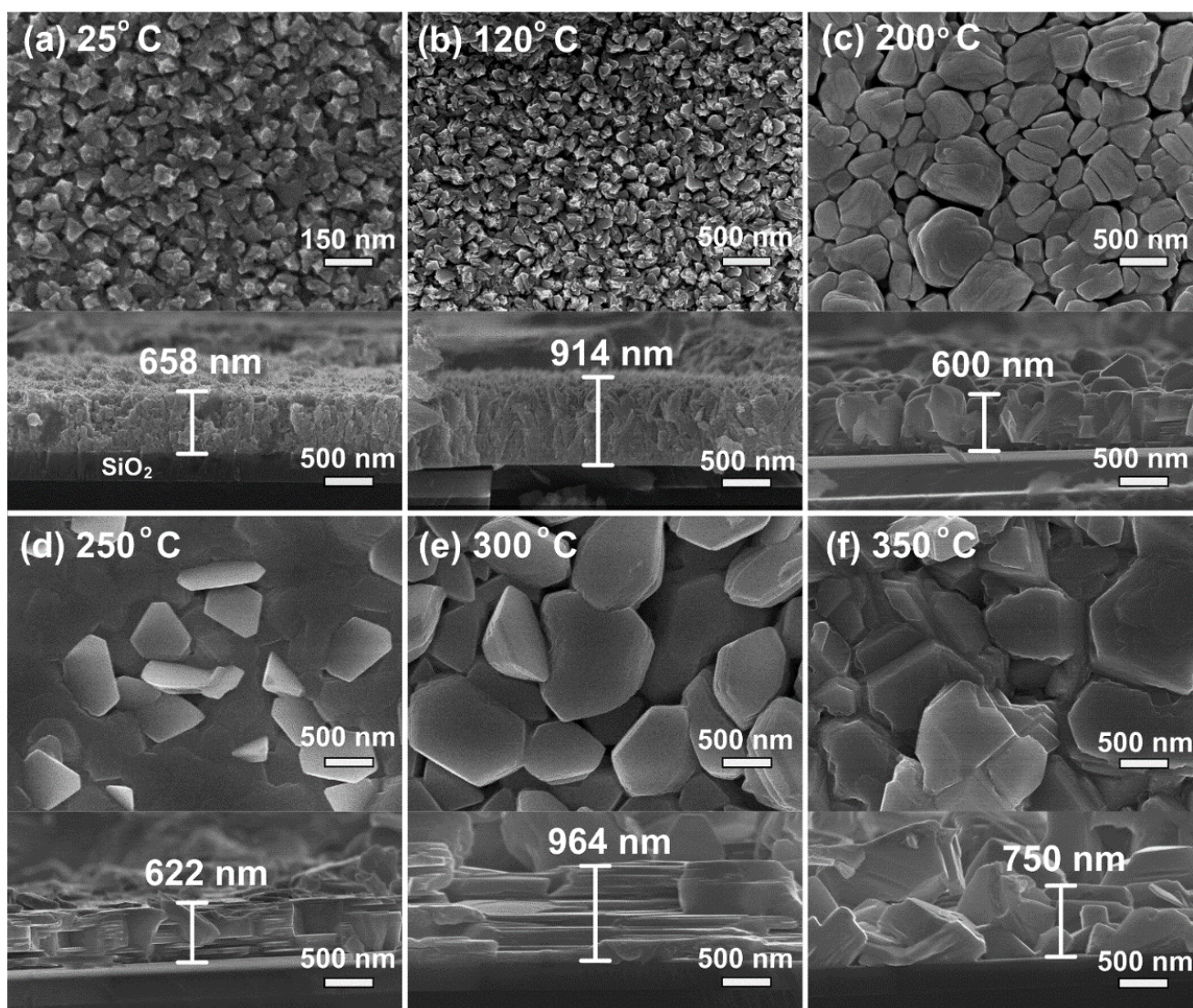


Figure 3. SEM images of the Bi-Te films grown at various substrate temperature (T_S) from 25°C to 350°C.

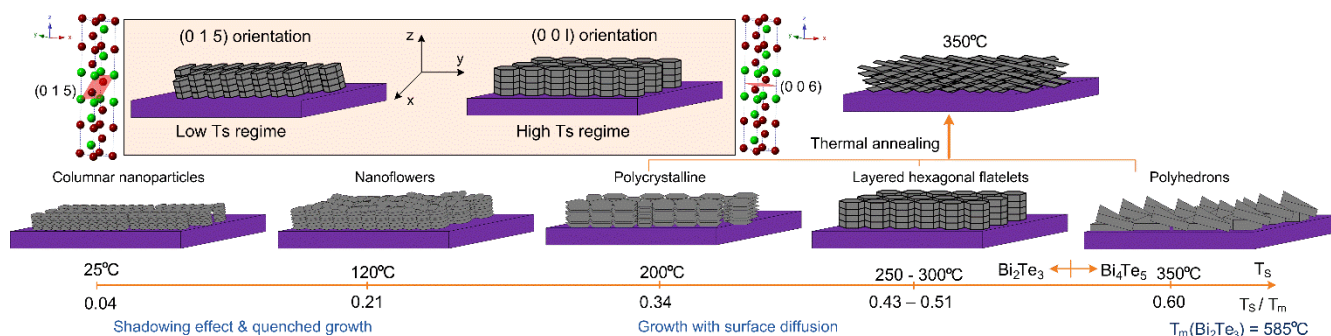


Figure 4. Thin-film growth schematic of Bi-Te thin films at various T_S from 25 to 350°C.

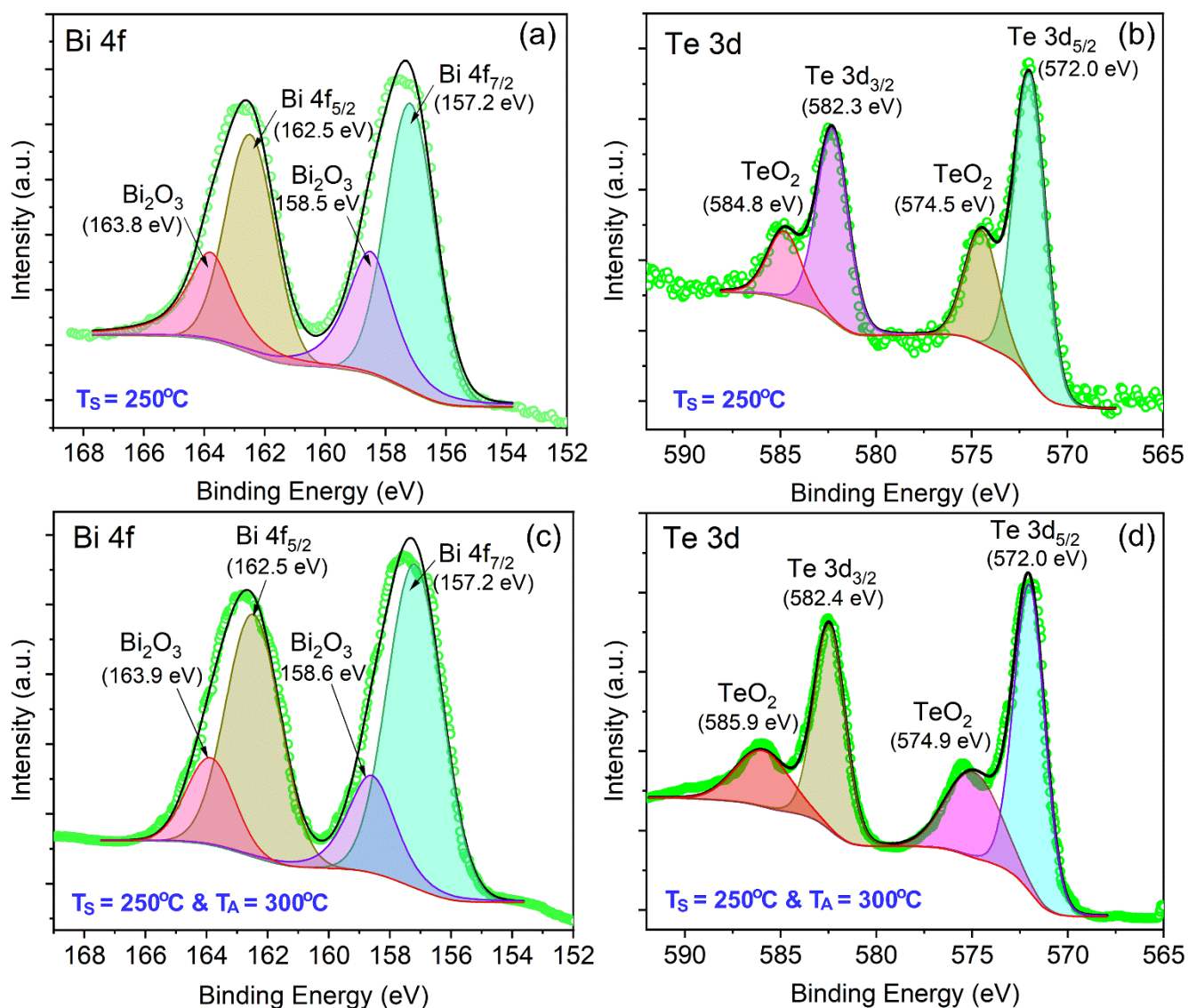


Figure 5. XPS spectra of the Bi 4f and Te 3d core levels for (a, b) the Bi_2Te_3 thin film grown at $T_S = 250^\circ\text{C}$, and (c, d) the Bi_2Te_3 film grown at $T_S = 250^\circ\text{C}$ followed by in-situ thermal annealing at $T_A = 300^\circ\text{C}$ for 1 h. All XPS measurements were conducted after five days of exposure to ambient atmosphere. Solid lines denote the fitted curves.

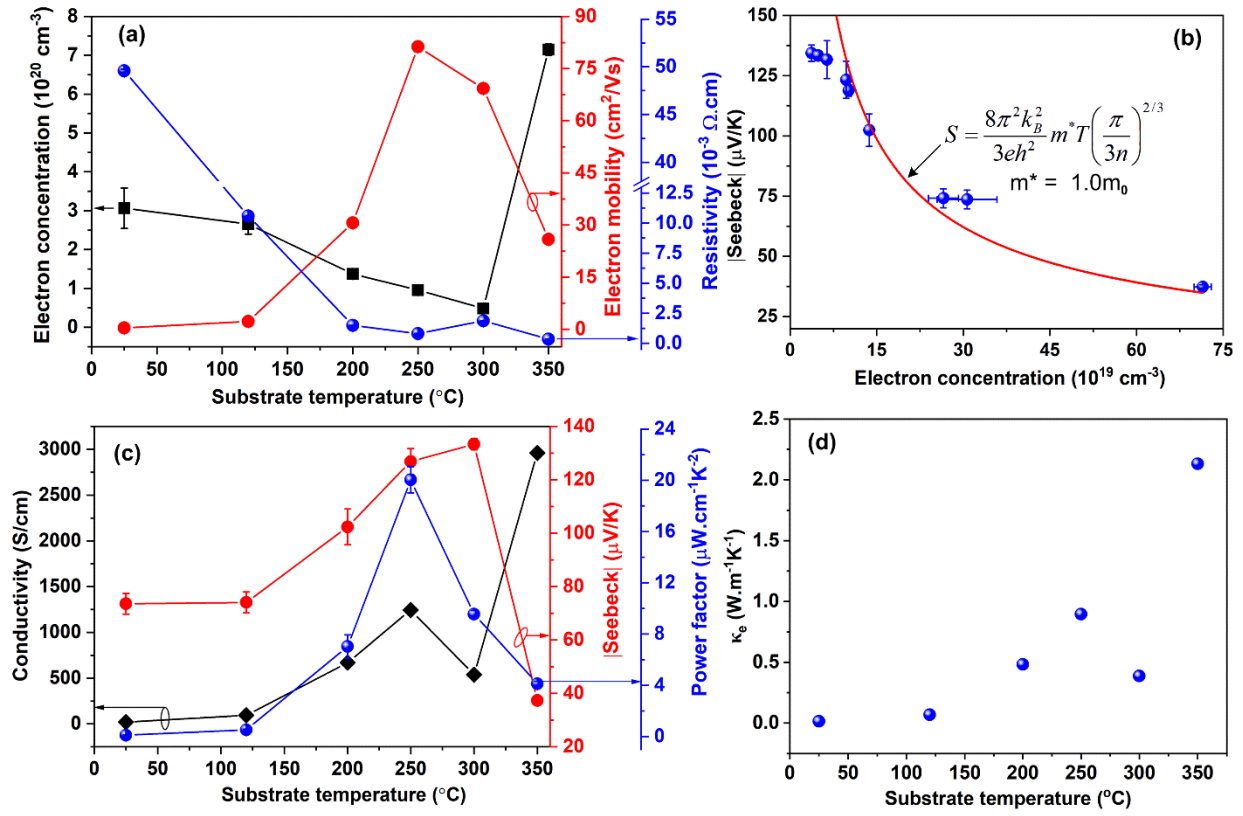


Figure 6. (a) T_S dependence of electron concentrations (n), electron mobility (μ) and resistivity (ρ). (b) Absolute Seebeck coefficient $|S|$ vs. n ; the solid lines are the plots of the Eq. (1), $|S| \sim m^* n^{-2/3}$, m_0 is the free electron mass. (c) T_S dependence of electrical conductivity (σ), Absolute Seebeck coefficient, and power factor ($\text{PF} = S^2\sigma$). (d) Electronic part of thermal conductivity for Bi-Te films grown at various T_S .

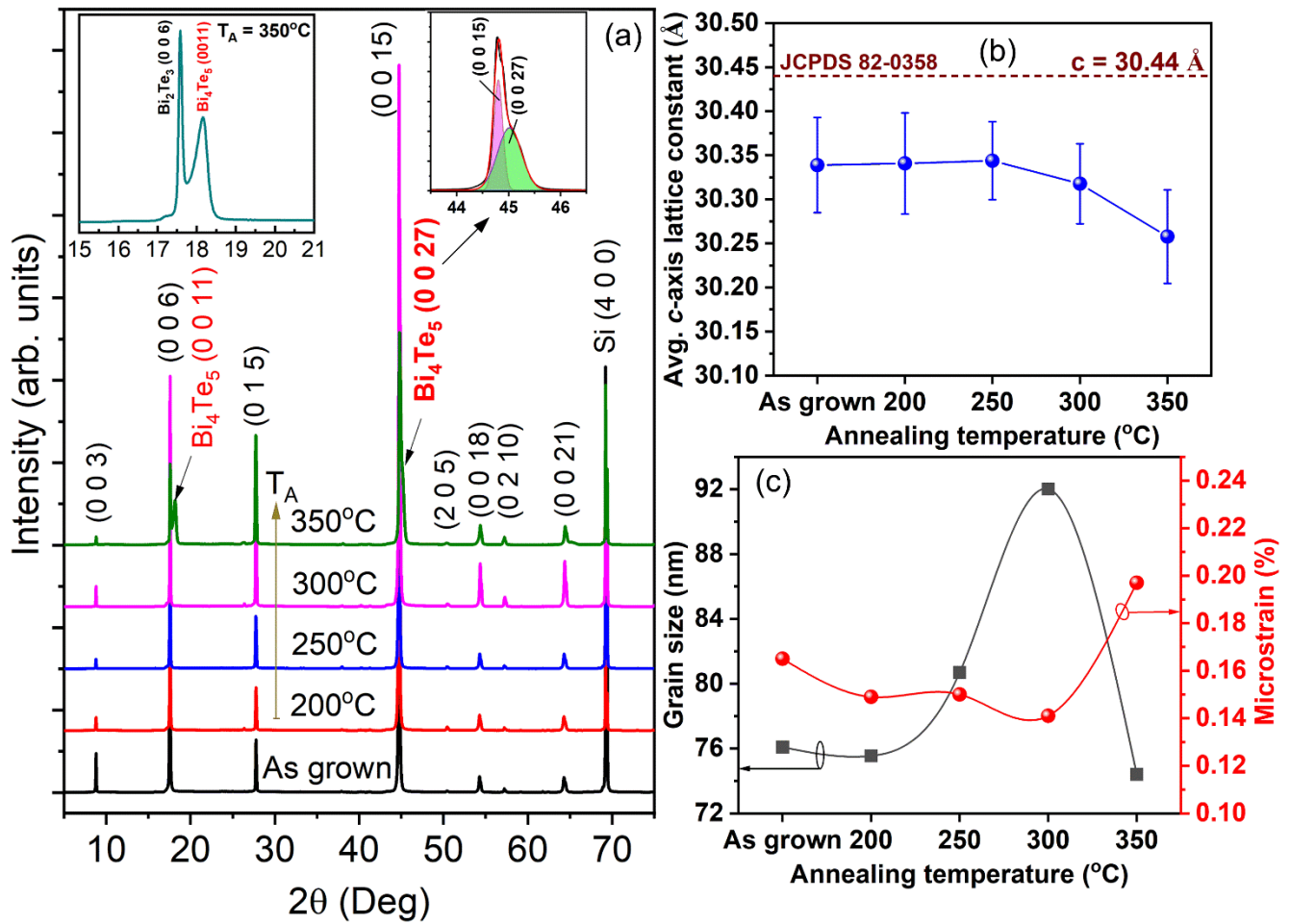


Figure 7. (a) XRD patterns of the Bi₂Te₃ thin film grown at 250°C and after *in-situ* thermal annealing at various temperatures (T_A) from 200°C to 350°C. The insets in (a) present zoom-in-view of two highest intensity peaks for the film annealed at 350°C. (b) T_A -dependent c -axis lattice constant of the Bi₂Te₃ thin films. (c) T_A -dependent grain size and microstrain of the films analysed by Williamson-Hall method.

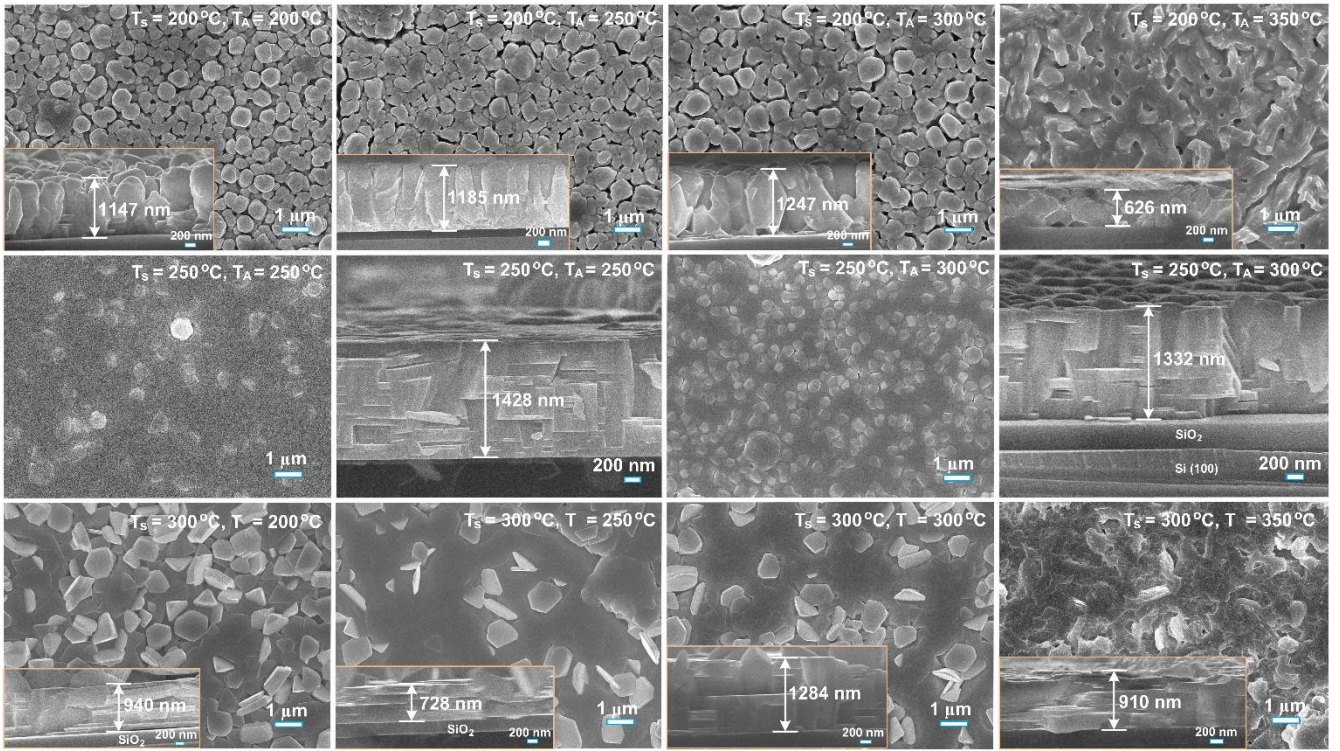


Figure 8. Plan-view and cross-sectional SEM images of Bi_2Te_3 films deposited at T_s of 200°C, 250°C, and 300°C, followed by *in-situ* thermal annealing at various temperatures (T_A) from 200°C to 350°C.

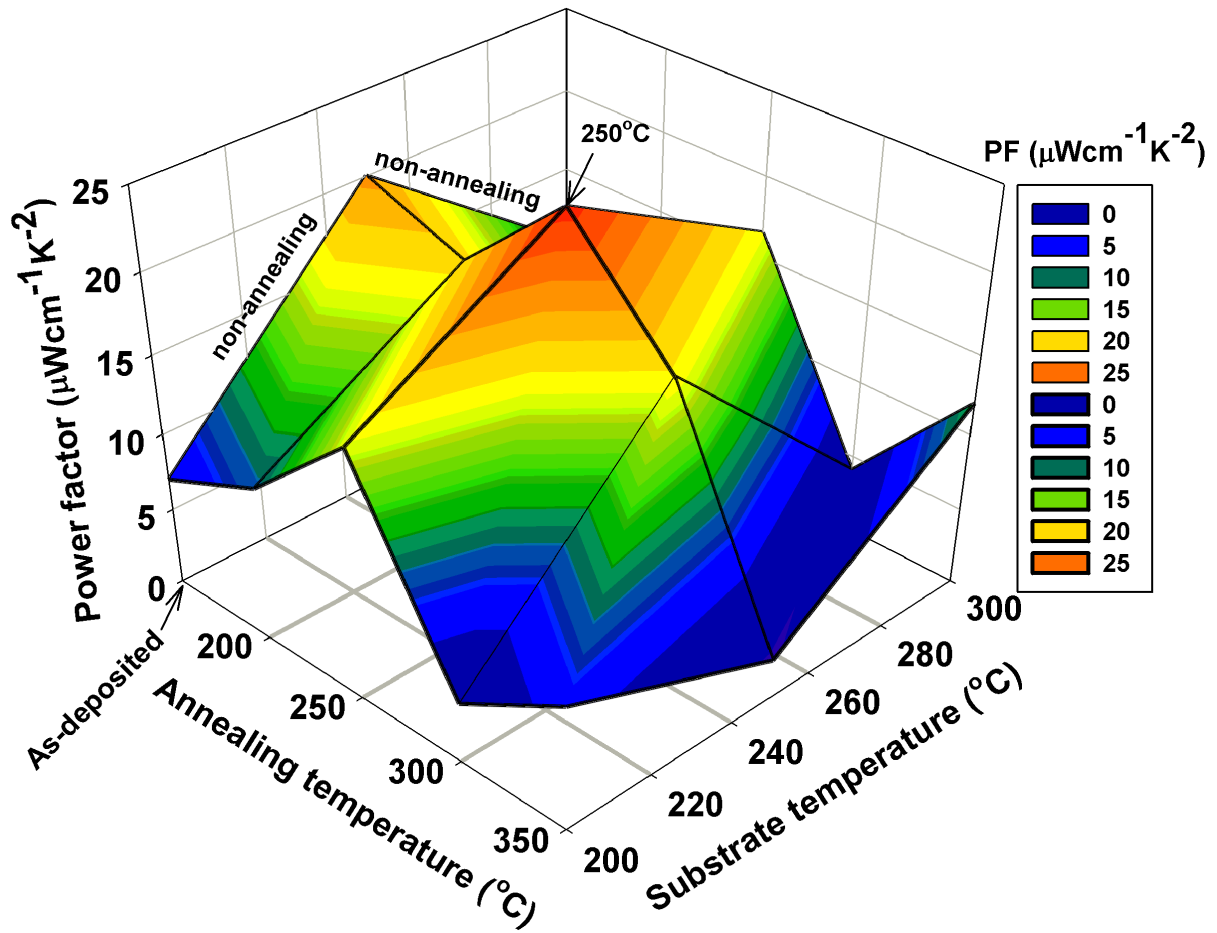


Figure 9. 3D contour plot of the film's power factor ($\text{PF} = S^2\sigma$) as functions of substrate temperature (T_S) of 200 – 300 $^{\circ}\text{C}$ and annealing temperature (T_A) of 200 – 350 $^{\circ}\text{C}$.

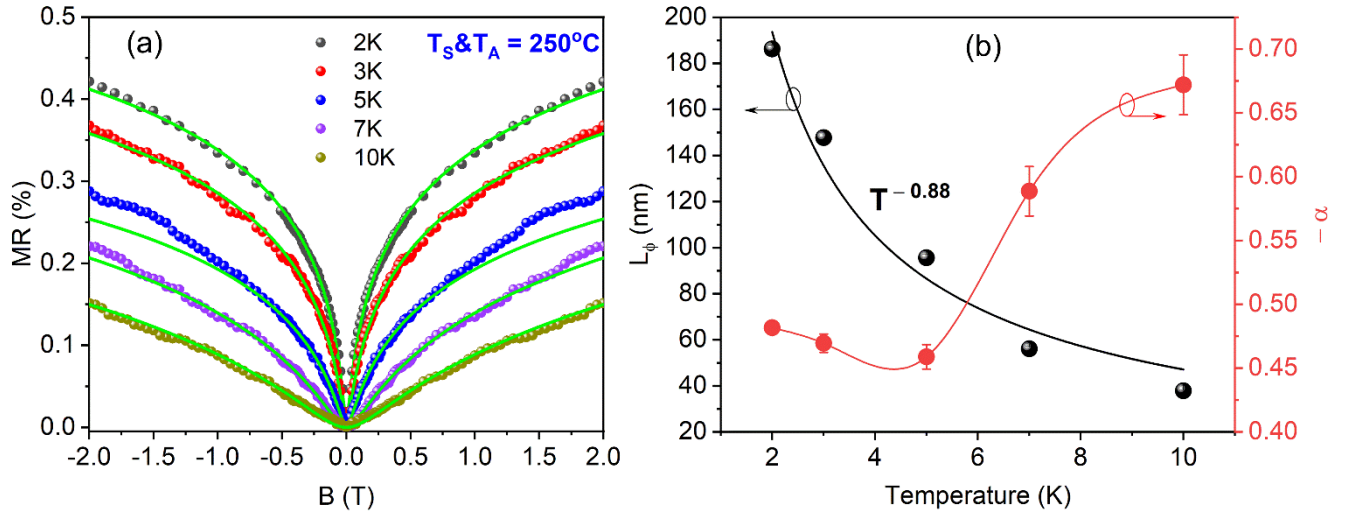


Figure 10. (a) Low-temperature magnetoresistance (MR, ± 2.0 T, 2 – 10 K) curves of the optimized Bi_2Te_3 thin film deposited and in-situ annealed at 250°C . The solid green lines at low magnetic fields represent the theoretical fits based on the 2D weak antilocalization (WAL) model using Eq. (4). (b) Temperature dependence of the extracted electron dephasing length L_ϕ and the parameter $-\alpha$. The solid fitting curve shows the power-law dependence of $L_\phi(T)$ with temperature.

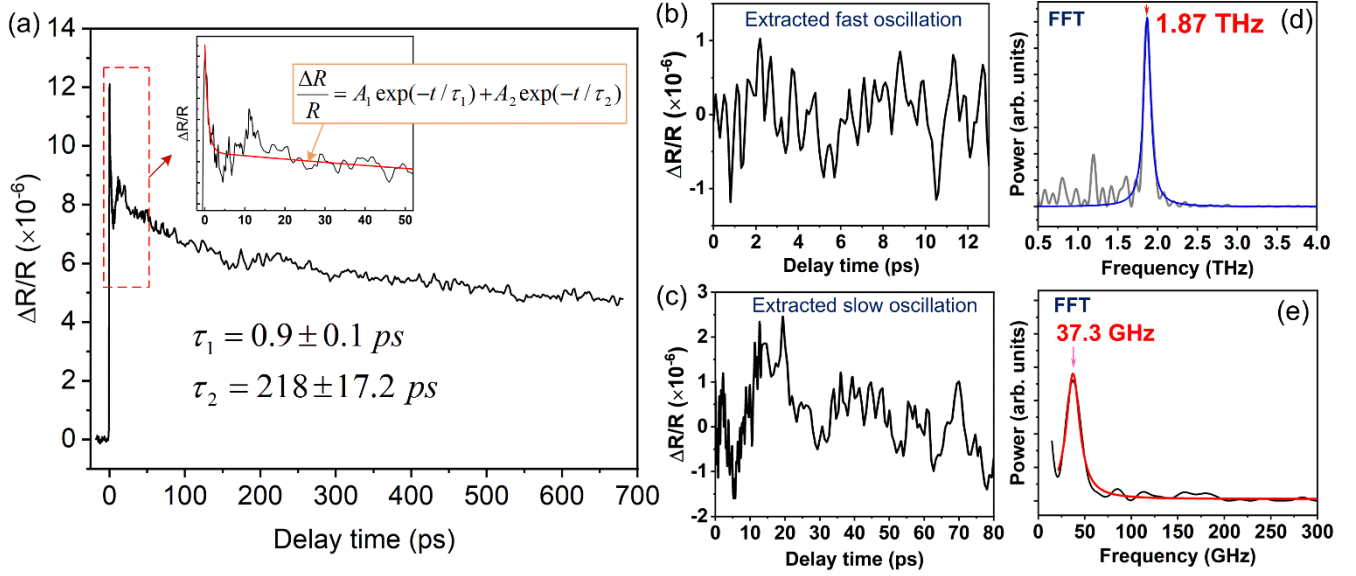


Figure 11. Room-temperature transient reflectivity change ($\Delta R/R$) spectrum of the optimized Bi_2Te_3 thin film deposited at $T_S = 250^\circ\text{C}$ and $T_A = 250^\circ\text{C}$. The inset shows a magnified view of the signal and its corresponding fit using Equation (5) over the range of -5 ps to 52 ps . Panels (b) and (c) display the extracted fast and slow oscillatory components, respectively. Panels (d) and (e) present the coherent optical and acoustic phonon frequencies, obtained via fast Fourier transform (FFT) analysis of the oscillations in (b) and (c).